**Radial breathing mode resonance Raman
cross-section analysis in single-walled carbon
nanotubes**

Pedro Barros Cotta Pesce

April 6, 2012

Radial breathing mode resonance Raman cross-section analysis in single-walled carbon nanotubes

Pedro Barros Cotta Pesce

Orientador: Prof. Ado Jório de Vasconcelos

Dissertação apresentada à Universidade Federal de Minas Gerais como requisito parcial para a obtenção do grau de Mestre em Física.

April 6, 2012

Aos meus pais, Lairson e Tina, e meus avós, Tuica, Meire e Matlédio.
Fizeram de mim quem sou hoje.

Acknowledgments

Considerando esta dissertação como resultado de um percurso que não começou na universidade, agradecer pode não ser tarefa fácil. Para não correr o risco da injustiça, agradeço irrestritamete a todos que, de uma forma ou de outra, contribuiram para minha formação. Destaco aqui apenas algumas das pessoas a quem sou especialmente grato.

Agradeço à minha família pelo carinho e apoio incondicional por toda minha vida. Também agradeço à Marina pela presença fundamental e constante, mesmo de longe.

Ao professor Marcos Prado, agradeço por despertar ainda no colégio a paixão pela física. Aos colegas Pauline e Adriano, obrigado pela coragem, por não ter que perseguir essa paixão sozinho.

Agradeço ao Ado pelo exemplo de ética de trabalho, pelos conselhos e compreensão nas decisões fáceis e difíceis, pelas conversas esclarecedoras e pelo direcionamento ao longo dessa pesquisa. Além de professor e orientador, teve que ser também psicólogo, conselheiro e líder de torcida ao longo dos altos e baixos de minha passagem pela UFMG.

Aos professores da UFMG, agradeço pelas excelentes aulas, pelo ambiente estimulante, estressante, mas extremamente agradável. Agradeço de maneira especial ao Mário Sérgio (por mostrar que tudo na física surge de maneira natural), ao Marcos Pimenta (por mais *insights* físicos do que eu seria capaz de listar), ao Dickman (por mostrar que existe **muita** física além das aproximações lineares), ao Schor (pelos breves, mas valiosos, passeios pela física matemática) e ao Bernardo Nunes, do Departamento de Matemática (que não sabe disso, mas foi uma das pessoas que mais me empolgou com o mundo das ciências exatas).

Agradeço profundamente ao grupos de colaboradores de outras instituições, nas figuras de Riichiro Saito, Pasha Nikolaev, Stephen Doorn, Millie Dresselhaus e Kenji Hata, sem os quais essa dissertação só teria páginas em branco a partir do capítulo 3.2.

Agradeço também ao INMETRO, nas figuras de Erlon Ferreira e Carlos Achete, pelo interesse na técnica e oportunidades oferecidas.

Agradeço aos Ramanistas (do Raman, do Near-Field e agregados) pela amizade, companheirismo e por tornarem agradáveis longos dias de medidas em laboratórios escuros, frios e apertados.

Aos amigos do Sete Verde, agradeço pelos momentos de descontração e pelas discussões, sempre relevantes, na sala do café, no DA, na sala de estudos, na sala de aula ou mesmo na mesa de bar. A esses e também aos demais colegas de curso, sou grato por compartilharem comigo o conhecimento e as dúvidas ao longo dos anos.

Agradeço aos amigos do Colégio Santo Antônio, companheiros de longa data, por manterem os momentos mais agradáveis do passado ainda presentes. Não é o carro voador que a gente queria, mas quem sabe essa pesquisa não é um passo nessa direção...

Contents

Resumo

Amostras de nanotubos de carbono de parede única (SWNT) geralmente são compostas por uma mistura de um grande número de diferentes espécies de SWNTs, cujas diferentes propriedades podem ser determinadas a partir de um par de índices (n, m), ou, equivalentemente, pelo seu diâmetro e ângulo quiral (d_t, θ). Aqui, utilizamos a espectroscopia Raman ressonante (RRS), uma técnica amplamente usada para a caracterização de amostras de SWNTs, para obter quantitativamente a distribuição de diâmetros de uma amostra. Para tanto, nos concentramos no modo Raman referente à vibração no modo de respiração radial (RBM) dos SWNTs, que, a partir de sua frequência e da energia de excitação utilizada, pode ser univocamente associado a uma única espécie de SWNT. Sua intensidade não depende apenas da abundância daquela determinada espécie de SWNT, mas também da eficiência com a qual o SWNT causa o espalhamento Raman (sua seção de choque RBM). Combinando medidas de microscopia eletrônica de transmissão de alta resolução (HRTEM) e de RRS em uma mesma amostra padrão de SWNTs, pudemos determinar e calibrar a seção de choque RBM dos SWNTs. Assim, propomos agora um método para determinar a distribuição de diâmetros de amostras de SWNTs utilizando apenas RRS.

Abstract

Single-walled carbon nanotubes (SWNT) samples usually consist of a mixture of several different SWNT species, whose different properties can be determined from a pair of indices (n, m), or, equivalently, from its diameter and chiral angle (d_t, θ). Here, we use resonance Raman spectroscopy (RRS), a technique widely used for the characterization of SWNT samples, to quantitatively determine the diameter distribution of such a sample. In order to do this, we focus on the Raman feature associated with the radial breathing mode (RBM) vibration of the SWNTs, which, given its frequency and the excitation wavelength, can be uniquely associated with a single SWNT species. Its intensity depends not only on the abundance of its related species, but also on the efficiency with which the SWNT causes Raman scattering (its RBM cross-section). By combining high resolution transmission electron microscopy (HRTEM) and RRS on the same standard SWNT sample, we calibrated and determined the RBM cross-section of a wide variety of SWNT species. Thus, we propose a method for the determination of the diameter distribution of any SWNT sample with only RRS measurements.

Chapter 1

Introduction

Nanometer-scaled materials are now commonplace in modern industrialized goods, with applications across the spectrum of human activities [1, 2, 3, 4, 5, 6]. One such material worthy of note are single-walled carbon nanotubes (SWNT), with promising applications in fields as diverse as energy storage [7], molecular diodes and transistors [8, 9, 10], gas sensors [11], the manufacture of strong and light-weight composite materials [12, 13, 14], among others [13, 14]. Though grouped under the common designation of SWNT, carbon nanotubes are in fact a collection of different species, each characterized by a pair of indices (n,m), which determine the SWNT's properties, such as its optical transition energies, or whether it is metallic or semiconducting [15, 16].

One of the requirements for the widespread commercial application of any material is the ability to efficiently and effectively assess the properties of a sample of material. Resonance Raman spectroscopy (RRS) has been used extensively [17, 18, 19, 20, 21] as a non-destructive tool to characterize isolated or bundled SWNT samples. By cross-referencing the optical transition energy (E_{ii}) and the frequency of the radial breathing mode (ω_{RBM}), determined by RRS measurements, we can assign (n, m) indices to the SWNTs present in the studied sample, since each RBM feature can be attributed to a different (n, m) species. The intensity of a RRS RBM feature depends on both the number of scatterers – the abundance of its related (n, m) species in the sample – and the RRS RBM cross-section for the SWNT species. Therefore, it can be used to determine the relative population of each probed (n, m) SWNT species within the sample.

However, theoretical [22, 23, 24] and experimental [17, 18, 21, 25, 26, 27, 28] efforts

to determine a SWNT sample's (n, m) population distribution have relied strongly on the assumed models for quantifying the photophysics of SWNTs. Luo *et al.* have obtained SWNT population information by combining fluorescence and absorption spectroscopy [17], as well as by observing the intensity of the Raman RBM overtone, while assuming the exciton-photon coupling dominates the Raman RBM cross-section [18]. Jorio *et al.* [21, 26] obtain the (n, m) populations of a sample based on the ratio of the observed Raman RBM intensity to the theoretical value obtained by a non-orthogonal tight-binding model. Okazaki *et al.* [25] compares experimental photoluminescence intensities with those calculated by an extended tight-binding model in order to obtain a sample's (n, m) population, while at the same time attempting to validate their results by comparing the photoluminescence-determined population with a diameter distribution obtained by transmission electron microscopy of around 100 SWNTs. Thus, it became clear to us that a more model-independent study of how the RRS RBM intensity depends on (n, m), as well as a characterization of the population distribution of a SWNT sample was lacking.

By combining high resolution transmission electron microscopy (HRTEM) of 395 SWNTs and RRS measurements on the same sample, we are able to calibrate the RRS RBM cross-section. In order for this calibration to be as general as possible, we chose a SWNT sample produced by water-assisted chemical vapor deposition ("super-growth"), which yields a vertical forest of nearly isolated, high purity SWNTs [20, 28, 29, 30, 31]. The characteristics of this sample, as determined by several RRS measurements [20, 29, 30], are close to those expected from ideal free-standing, isolated SWNTs. In particular, it shows the highest E_{ii} reported in the literature and a strict adherence to the relation $\omega_{\mathrm{RBM}} = 227/d_t$ nm $\cdot$ cm^{-1}, indicating negligible environmental influence on the SWNTs' behavior.

This calibration allows us to determine the diameter distribution of a given sample in a non-destructive way, using only RRS measurements. It is hoped that this will be instrumental for the widespread commercial use of SWNT.

Chapter 2

Single-Walled Carbon Nanotubes

2.1 Geometrical description

Single-walled carbon nanotubes (SWNT) are a specific arrangement of carbon atoms which can be described as a single graphene sheet rolled up into a cylinder. A SWNT is uniquely characterized by its chiral vector $(\vec{C_h})$ [32], which connects the atoms in the graphene lattice which are seamlessly sewn together during this hypothetical roll-up. In order to obtain a seamless cylinder, $\vec{C_h}$ must be written as:

$$\vec{C_h} = n\vec{a_1} + m\vec{a_2} \tag{2.1}$$

where $\vec{a_1}$ and $\vec{a_2}$ are the graphene lattice vectors and (n, m) are integers which determine $\vec{C_h}$ and, therefore, the SWNT's properties.

As $\vec{C_h}$ spans the circumference of the cylinder, we can obtain the SWNT's diameter (d_t) as:

$$d_t = \frac{|\vec{C_h}|}{\pi} = \frac{\sqrt{n^2|\vec{a_1}|^2 + 2nm(\vec{a_1} \cdot \vec{a_2}) + m^2|\vec{a_2}|^2}}{\pi} = \frac{a_{c-c}}{\pi}\sqrt{3(n^2 + nm + m^2)} \tag{2.2}$$

where $a_{c-c} = 1.42$Å is the distance between neighboring carbon atoms in graphene and n, m are integers.

Another useful parameter is the chiral angle (θ), which is defined as the angle

3

between $\vec{C_h}$ and $\vec{a_1}$:

$$\tan\theta = \frac{|\vec{a_1} \times \vec{C_h}|}{|\vec{a_1} \cdot \vec{C_h}|} = \frac{m\sqrt{3}}{m + 2n} \tag{2.3}$$

SWNTs with $\theta = 0°$ or $\theta = 30°$ are termed *zig-zag* and *armchair*, respectively, due to the characteristic shapes of the C-C bonds along these directions. SWNTs with $0° < \theta < 30°$ are termed *chiral*.

In addition to the circumferential "periodicity" described by $\vec{C_h}$, SWNTs are periodic in the traditional sense of the word along their axis. The translation vector $\vec{T}$ which connects two equivalent carbon atoms along the SWNT axis can be written as:

$$\vec{T} = t_1\vec{a_1} + t_2\vec{a_2} \tag{2.4}$$

for adequate integers t_1 and t_2. Since $\vec{T}$ is parallel to the SWNT axis, it is perpendicular to $\vec{C_h}$:

$$\begin{aligned}
0 &= \vec{C_h} \cdot \vec{T} \\
0 &= nt_1|\vec{a_1}|^2 + (nt_2 + mt_1)(\vec{a_1} \cdot \vec{a_2}) + mt_2|\vec{a_2}|^2 \\
0 &= t_1(2n + m) + t_2(n + 2m)
\end{aligned} \tag{2.5}$$

The smallest t_1 and t_2 which satisfy (2.5) are:

$$t_1 = \frac{n + 2m}{d_R} \quad ; \quad t_2 = -\frac{2n + m}{d_R} \tag{2.6}$$

where d_R is the greatest common divisor of $(2n + m, n + 2m)$.

The vectors $\vec{C_h}$ and $\vec{T}$ define the SWNT unit cell, as can be seen in figure 2.1. The ratio of the area of the SWNT unit cell to that of graphene gives us the number of hexagons (N) in the unit cell of a SWNT:

$$N = \frac{|\vec{C_h} \times \vec{T}|}{|\vec{a_1} \times \vec{a_2}|} = \frac{2(n^2 + nm + m^2)}{d_R} \tag{2.7}$$

Since each hexagon contains two unique carbon atoms, the number of atoms in the SWNT unit cell is $2N$.

Thus, we can describe the geometry of a SWNT species either by (n, m), or (d_t, θ), which will be done interchangeably throughout this text.
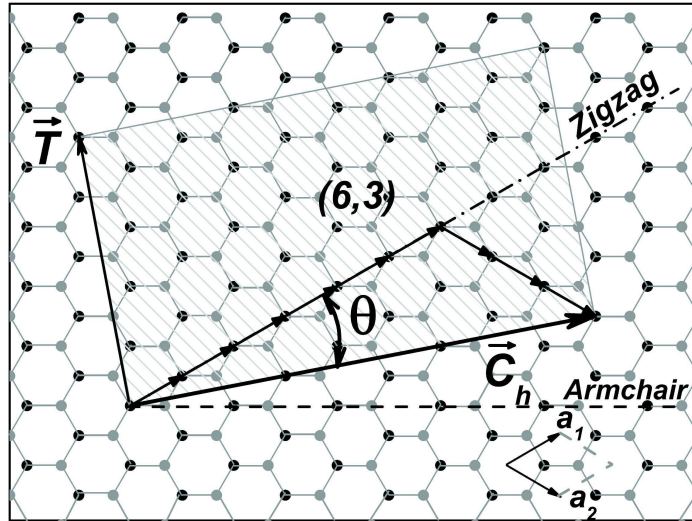
Figure 2.1: The chiral vector $\vec{C_h}$ and the translation vector $\vec{T}$ for the (6,3) SWNT, superimposed on a graphene lattice. The dashed rectangle is the (6,3) SWNT unit cell. [33]

2.2 Electronic properties

In much the same way as a SWNTs' geometrical structure can be described as a graphene lattice over which we superimposed the periodicity of the chiral vector $\vec{C_h}$ and the translation vector $\vec{T}$, so too can is its electronic structure, as a first approximation, be described as that of graphene plus the SWNT's periodicity requirements. This description gives rise to the picture of *cutting lines* throughout the first Brillouin zone of graphene, which describe the wavevectors available to SWNTs. This approach fails to address the effects of curvature, as well as excitonic and many-body effects, which distort the calculated energy levels, but is enough to give us much insight into the physics at hand.

2.2.1 Tight-binding approximation for graphene

As a first description, let us take graphene's electronic structure near the Fermi level as calculated by a first neighbors tight-binding approximation. This is a perturbative approach in which the unperturbed eigenvectors are taken as the relevant atomic orbitals – carbon's $2p_z$ orbital, denoted by φ_z here – and the crystal's potential is the perturbation [15]. The two inequivalent carbon atoms – here indexed as A and B – in graphene's unit

cell give rise to two Bloch functions:

$$\Phi_{A,B} = \frac{1}{\sqrt{M}} \sum_{\ell=1}^{3} e^{i\vec{k}\cdot\vec{R_\ell}} \varphi_z(\vec{r} - \vec{R_\ell}) \tag{2.8}$$

where M is the number of unit cells in the crystal and $\ell = 1, 2, 3$ represents the three first neighbors of the relevant carbon atom. The interaction Hamiltonian ($\mathcal{H}$) and the overlap integral matrix for this system are hermitian and symmetric to a changing of indexes $A \leftrightarrow B$, and depend only on the sum of the phase factors ($f(\vec{k}) = \sum_{\ell} e^{i\vec{k}\cdot\vec{R_\ell}}$), being of the form:

$$\mathcal{H} = \begin{pmatrix} \varepsilon_{2p} & -\gamma_0 f(\vec{k}) \\ -\gamma_0 f^\star(\vec{k}) & \varepsilon_{2p} \end{pmatrix} \quad ; \quad \mathcal{S} = \begin{pmatrix} 1 & sf(\vec{k}) \\ sf^\star(\vec{k}) & 1 \end{pmatrix} \tag{2.9}$$

where ε_{2p} is the energy of the atomic $2p_z$ orbital, γ_0 is the nearest-neighbor transfer integral and s is the nearest-neighbor overlap integral.

Obtaining the energy eigenvalues reduces to solving the secular equation:

$$\det\left(\mathcal{H} - E(\vec{k})\mathcal{S}\right) = 0 \tag{2.10}$$

where "det" denotes the determinant. This yields the familiar energy dispersion of graphene, which, with a suitable choice of a reference frame can be written as:

$$E(\vec{k}) = \frac{\varepsilon_{2p} \pm \gamma_0 w(\vec{k})}{1 \pm sw(\vec{k})} \quad ; \quad w(\vec{k}) = |f(\vec{k})| \tag{2.11}$$

2.2.2   Quantization in the electronic structure of SWNTs

Now that we have a basic description of the electronic structure of graphene, we must apply the periodicity imposed by the peculiar geometry of SWNTs [16]. Since our ideal SWNT is of infinite length, the wavevector along the direction of the SWNT axis is unconstrained, but the periodicity along the circumference of SWNTs restricts our choice of wavevectors to those that satisfy:

$$\vec{k} \cdot \vec{C_h} = \mu 2\pi \tag{2.12}$$

for integer μ. Note that $|\vec{C_h}| = \pi d_t$ and let

$$\vec{K_1} = \frac{2}{d_t} \frac{\vec{C_h}}{|\vec{C_h}|} \quad ; \quad \vec{K_2} = \frac{\vec{T}}{|\vec{T}|} \tag{2.13}$$
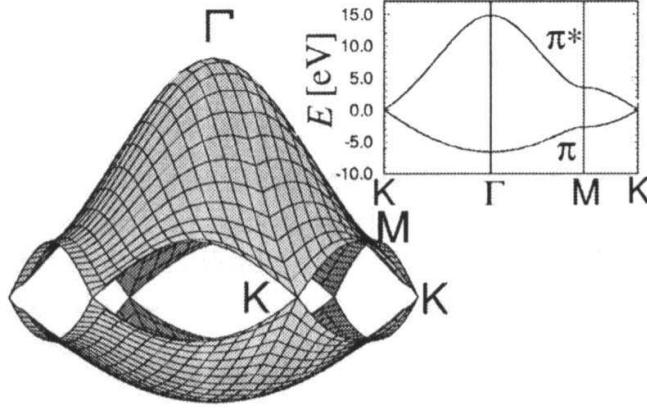
Figure 2.2: Graphene's electronic structure close to the Fermi energy, as calculated by the first-neighbor tight-binding approximation. The inset shows shows cuts along high-symmetry lines. Here, γ_0 and s are, respectively, 3.033 eV and 0.129. [15, 34]

thus we can write the allowed wavevectors of a SWNT as

$$\vec{k}_{\text{SWNT}} = \mu \vec{K_1} + k \vec{K_2} \tag{2.14}$$

where μ is an integer and k is a real number. However, since $N\vec{K_1}$ is also a vector of the graphene reciprocal lattice, we can limit the acceptable values to $\mu = 0, 1, \ldots, N-1$, limiting ourselves to the first Brillouin Zone (BZ). We can limit $-\pi/|\vec{T}| < k < \pi/|\vec{T}|$ in order to stay in the first BZ as well. Thus, we obtain the electronic energy dispersion of SWNTs near the Fermi level as

$$E_\mu(k) = \frac{\varepsilon_{2p} \pm \gamma_0 w(\vec{k}_{\text{SWNT}})}{1 \pm sw(\vec{k}_{\text{SWNT}})} \tag{2.15}$$

This gives rise to N pairs of bands of electronic states in the first BZ. However, N can be a rather large number, these bands are all within a few eV of each other and cross each other frequently, making the band structure rather confusing, as figure 2.3(b) shows. It is usually more instructive to look at the density of electronic states ($g(E)$), given by [16]:

$$g(E) = \frac{2}{N} \sum_{\mu=0}^{N-1} \int \left[\frac{dE_\mu(k)}{dk} \right]^{-1} \delta(E_\mu(k) - E) dk \tag{2.16}$$

One of the interesting properties of SWNTs is that, if one of the cutting lines crosses the K point of the graphene BZ, which happens only for $(2n + m) \bmod 3 = 0$ [15], the
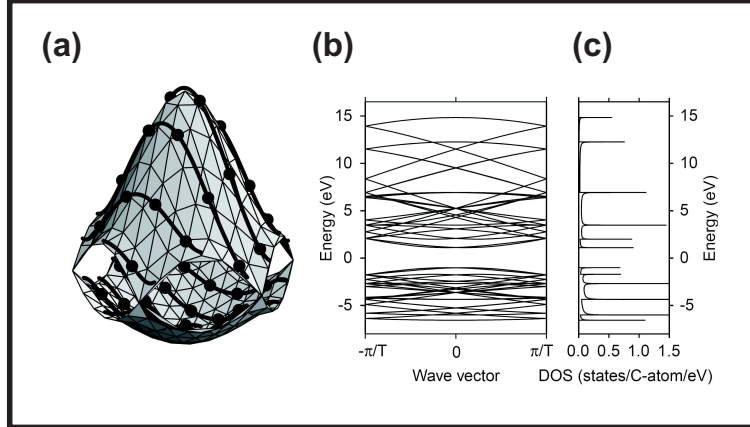
7

Figure 2.3: (a) Allowed electronic states for the $(4, 2)$ nanotube superimposed on graphene's π and $\pi^\star$ bands. Each segment delimited by black bullets represents a single energy band, as seen in (b). (b) Electronic energy bands for the $(4, 2)$ nanotube. (c) Density of electronic states for the band diagram in (b). [15, 34, 35]

SWNT has a non-zero $g(E)$ at the Fermi energy, meaning it is *metallic* (M). If this is not the case, the SWNT is *semiconducting* , and is classified as either *type 1* (S_1, for $(2n + m)\mathrm{mod}\,3 = 1$), or *type 2* ($S_2$, for $(2n + m)\mathrm{mod}\,3 = 2$).

Note that whenever $dE_\mu/dk = 0$, $g(E)$ diverges sharply. These local maxima in density of states (DOS) are called van Hove singularities (vHS) and are responsible for strong electronic transitions, causing SWNTs to behave almost like molecules and not traditional crystals, with discrete, rather than continuous energy levels. The energy difference between the i-th vHS in the valence band and the j-th vHS in the conduction band is dubbed $E_{ij}^{\mathrm{M,S}}$, for metallic (M) or semiconducting (S) SWNTs. Due to symmetry considerations, the interaction of light polarized along the SWNT axis – which couples much more strongly to the SWNT's electrons than other polarizations – can only promote transitions where $i = j$ [16, 32]. The transitions with smallest E_{ii} will occur close to the graphene K point, where the electronic dispersion is close to linear, and can be approximated by [15]:

$$E_{ii}(d_t, \theta) \approx a\frac{p}{d_t} + \beta_p\frac{\cos 3\theta}{d_t^2} \tag{2.17}$$

where β_p takes into account the weak angle dependence of the electronic dispersion, a is an adjustable parameter and $p = 1, 2, 3, 4, \ldots$ for $E_{11}^{\mathrm{S}}, E_{22}^{\mathrm{S}}, E_{11}^{\mathrm{M}}, E_{33}^{\mathrm{S}}, \ldots$.

Even though this simplistic approach can give us much physical insight, for several reasons it is not enough to quantitatively describe E_{ii}, especially for tubes with small d_t

[36]. The first of these reasons is that we only took into account first neighbors in equation (2.8), when realistically all neighbors must be accounted for. Also, when first calculating the tight-binding approximation for graphene, we used only one electron per carbon atom, since we were only interested in describing in the π bands, which are orthogonal to the σ bonds in planar graphene [15]. When we rolled up the graphene sheet to form the SWNT, this orthogonality was lost, but we did not take this into account in subsequent expressions. Both of these aspects can be adequately described by the so-called non-orthogonal extended tight-binding (ETB) [37, 38], in which both π- and σ-orbitals are considered, as well as the entire SWNT geometry. First, one considers as many neighbors as is practical for carbon atoms along the SWNT in order to obtain an approximate energy dispersion. Then, while being constrained by the helical symmetry of the specific SWNT one is interested in, the bonding angles between neighboring atoms are allowed to vary, lowering the total energy of the system.

While the ETB can accurately describe the SWNT band structure, it does not describe the excitonic nature of optical transitions in SWNTs [39, 40]. These effects can be calculated within the tight-binding approximation by solving the Bethe-Salpeter equation [41, 42], yielding both the excitonic wavefunctions and transition energies. Since electron-electron repulsion and electron-hole attraction (many-body effects) in SWNTs almost cancel out, they can be taken into account by a logarithmic correction [43, 44], given by:

$$E_{ii}(d_t, \theta) = a\frac{p}{d_t}\left(1 + b\log\frac{c}{p/d_t}\right) + \beta_p\frac{\cos 3\theta}{d_t^2} \tag{2.18}$$

where b is an adjustable parameter and $c = 0.812\text{nm}^{-1}$. Additionally, since the excitonic contribution is different for small and large ii [36], an extra term of $\gamma p/d_t$ must be added for transitions higher than E_{11}^{M} [36].

2.3 Vibrational properties

Similarly to the electronic structure, most of the SWNT's basic vibrational properties can be described in terms of graphene's vibrational properties, while respecting the symmetry imposed by the geometry of SWNTs [16]. However, the main vibrational mode of interest to us, the radial breathing mode (RBM), cannot be accurately described by this approach. The RBM is an oscillating symmetric radial displacement of the SWNT's atoms, and the

analogous displacement in graphene is merely a translation perpendicular to the graphene plane, with no associated restoring force. A simple model that predicts the basic behavior of the RBM is to consider the oscillation of a thin cylindrical shell of thickness h subjected to an inward pressure $p(x) = -Kx$ [45]:

$$\frac{\rho}{Y}(1 - \nu^2)\frac{\partial x(t)}{\partial t^2} + \frac{4}{d_t^2}x(t) = -\frac{(1 - \nu^2)}{Yh}Kx(t) \qquad (2.19)$$

where ρ is the cylinder's density, Y is its Young's modulus, ν is Poisson's ratio and $x(t)$ is a small radial displacement. Solving for an oscillating $x(t) = \exp(i\omega_{\text{RBM}}t)$ yields:

$$\omega_{\text{RBM}} = \sqrt{\frac{4Y}{\rho(1 - \nu^2)}\frac{1}{d_t^2} + \frac{K}{\rho h}}$$

$$\omega_{\text{RBM}} = \frac{A}{d_t}\sqrt{1 + C \cdot d_t^2} \qquad (2.20)$$

Where C is an environment-dependent constant [20] and both elasticity theory [46] and experimental measurements [20] give the value $A = 227\text{nm}\cdot\text{cm}^{-1}$. In free space ($p(x) = 0$), this is consistent with the familiar behavior of simple oscillating systems, where $\omega \propto \sqrt{(k/m)}$, since the total mass of the system is proportional to the circumference ($m \propto \rho d_t$) and the stiffness is inversely proportional to it, like in a system of springs connected in series ($k \propto Y/d_t$).

Chapter 3

Theoretical background

3.1 Raman scattering

3.1.1 Classical description

Classically, Raman scattering is caused by the modulation of a material's polarizability due to its vibrations [16]. An incident oscillating electric field $\vec{E}$ will induce a polarization $\vec{P}$ given by:

$$\vec{P} = \overleftrightarrow{\alpha}\vec{E} \tag{3.1}$$

where $\overleftrightarrow{\alpha}$ is the electric polarizability tensor, which is generally a function of the atomic positions of the system. For simplicity, let us assume the system is vibrating in a single normal vibrational mode Q. The polarizability can then be expanded around the equilibrium positions of the atoms as:

$$\overleftrightarrow{\alpha} = \overleftrightarrow{\alpha}_0 + \left.\frac{\partial \overleftrightarrow{\alpha}}{\partial Q}\right|_0 Q + \cdots \tag{3.2}$$

where the derivative is evaluated in the system's equilibrium configuration. Let Q and $\vec{E}$ be:

$$Q = Q_0 \cos(\omega_q t) \quad ; \quad \vec{E} = \vec{E}_0 \cos(\omega_I t) \tag{3.3}$$

Up to first order, equation (3.1) can then be written as:

$$\vec{P} = \overleftrightarrow{\alpha}_0 \vec{E}_0 \cos(\omega_I t) + \left.\frac{\partial \overleftrightarrow{\alpha}}{\partial Q}\right|_0 Q_0 \vec{E}_0 \cos(\omega_q t) \cos(\omega_I t) \tag{3.4}$$

Since $2\cos(a)\cos(b) = \cos(a + b) + \cos(a - b)$, this becomes:

$$\vec{P} = \overleftrightarrow{\alpha}_0\vec{E}_0 \cos(\omega_I t) + \frac{1}{2}\frac{\partial\overleftrightarrow{\alpha}}{\partial Q}\bigg|_0 Q_0\vec{E}_0\big[\cos(\omega_I + \omega_q)t + \cos(\omega_I - \omega_q)t\big] \qquad (3.5)$$

Thus, an incident monochromatic light of frequency ω_I will scatter elastically – Rayleigh scattering – and inelastically – Raman scattering – provided $(\partial\overleftrightarrow{\alpha}/\partial Q)_0 \neq 0$. The scattered light with frequencies $(\omega_I - \omega_q)$ and $(\omega_I + \omega_q)$ are referred to as Stokes and anti-Stokes scattering, respectively.

3.1.2   Quantum mechanical description

Within the framework of quantum mechanics, Raman scattering in crystals is the inelastic scattering of a photon by a phonon [16]. The most intuitive process that allows this scattering in a large crystal is one in which an incident photon of energy $\hbar\omega_I$ is absorbed by the crystal, promoting an electron to an excited state. In the Stokes process, before relaxing back to its ground state, the excited electron emits a phonon, losing $\hbar\omega_q$ energy. The excited electron then relaxes back to its original state by an optical transition, emitting a scattered photon of energy $\hbar\omega_S = \hbar\omega_I - \hbar\omega_q$. This process is illustrated schematically in figure 3.1.
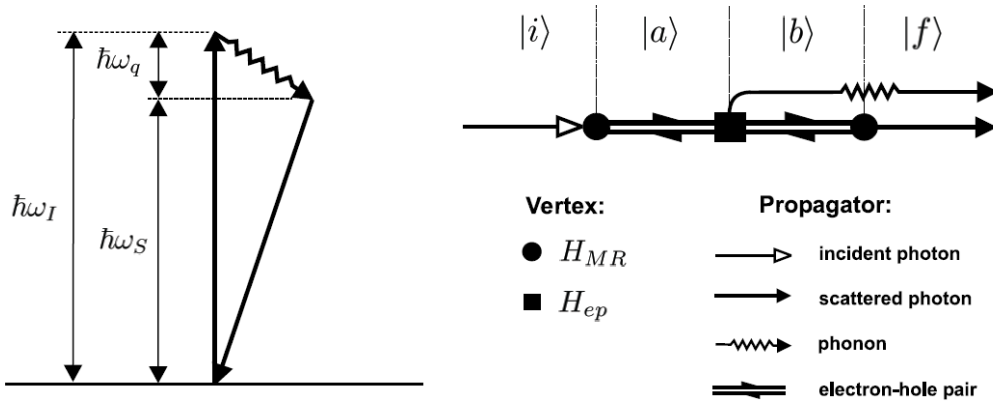

Figure 3.1: Schematic representation of the energy levels and the Feynmann diagram for the Stokes process in Raman scattering. An electron is excited by an incident photon $\hbar\omega_I$, emits a phonon $\hbar\omega_q$ and relaxes by emitting a photon of energy $\hbar\omega_S = \hbar\omega_I - \hbar\omega_q$. [47]

The probability for this scattering to occur is described by third-order time-dependent perturbation theory [15, 16, 33, 34, 47, 48, 49]. Here, instead of deducing the expression for the scattering probability, we shall concentrate on an analysis of the description of the system and the use of the end result for calculating RBM Raman intensities in SWNTs. In order to apply perturbation theory, we define the Hamiltonian of the system as $\mathcal{H} = \mathcal{H}_0 + \mathcal{H}_1$, where:

$$\begin{aligned} \mathcal{H}_0 &= \mathcal{H}_M + \mathcal{H}_R \\ \mathcal{H}_1 &= \mathcal{H}_{MR} + \mathcal{H}_{ep} \end{aligned} \tag{3.6}$$

such that $\mathcal{H}_0 \gg \mathcal{H}_1$ and $\mathcal{H}_1$ is treated as a perturbation. Here, $\mathcal{H}_M$ and $\mathcal{H}_R$ represent the Hamiltonians for the matter and radiation parts of the system, respectively, and $\mathcal{H}_{MR}$ and $\mathcal{H}_{ep}$ describe the matter-radiation and exciton-phonon couplings, respectively. The process illustrated in figure 3.1 involves four eigenstates of $\mathcal{H}_0$: the initial state $|i\rangle$, two intermediate states $|a\rangle$ and $|b\rangle$, and the final state $|f\rangle$. An eigenstate with eigenvalue E_x is described as $|x\rangle = |n_I, n_S, n_q, \varphi_x\rangle$, where n_I is the number existing incident photons, n_S is the number of existing scattered photons, n_q is the number of existing phonons and φ_x is the electron's state. The relevant states and their eigenvalues are then:

$$\begin{aligned} |i\rangle &= | \quad n_I \quad , \quad n_S \quad , \quad n_q \quad , \varphi_i \rangle \\ |a\rangle &= | \ n_I - 1 \ , \quad n_S \quad , \quad n_q \quad , \varphi_a \rangle \\ |b\rangle &= | \ n_I - 1 \ , \quad n_S \quad , \ n_q + 1 \ , \varphi_b \rangle \\ |f\rangle &= | \ n_I - 1 \ , \ n_S + 1 \ , \ n_q + 1 \ , \varphi_f \rangle \end{aligned} \tag{3.7}$$

and their eigenvalues are:

$$\begin{aligned} E_i &= \quad n_I \hbar\omega_I \quad + \quad n_S \hbar\omega_S \quad + \quad n_q \hbar\omega_q \quad + E_i^e \\ E_a &= (n_I - 1)\hbar\omega_I + \quad n_S \hbar\omega_S \quad + \quad n_q \hbar\omega_q \quad + E_a^e \\ E_b &= (n_I - 1)\hbar\omega_I + \quad n_S \hbar\omega_S \quad + (n_q + 1)\hbar\omega_q + E_b^e \\ E_f &= (n_I - 1)\hbar\omega_I + (n_S + 1)\hbar\omega_S + (n_q + 1)\hbar\omega_q + E_f^e \end{aligned} \tag{3.8}$$

where E_x^e is the energy of the electronic state described by φ_x.

The standard time-dependent perturbation theory formalism gives the Raman cross-section for this process as [47]:

$$\sigma = C \sum_f \left| \sum_{a,b} \frac{\langle f|\mathcal{H}_{MR}|b\rangle \langle b|\mathcal{H}_{ep}|a\rangle \langle a|\mathcal{H}_{MR}|i\rangle}{(E_i - E_a)(E_i - E_b)} \right|^2 \delta(E_i - E_f) \tag{3.9}$$

where C depends on the incident light source and the material's refraction index.

Whenever the denominator in equation (3.9) approaches zero, the cross-section becomes very large. This phenomenon is referred to as resonance Raman scattering (RRS) and, when present, dominates over non-resonant scattering. RRS will occur whenever the energy of either the incident or scattered photons matches a SWNT's E_{ii} optical transition energy. As written, the right hand side of equation (3.9) diverges whenever either resonance condition is achieved, but this is unphysical. Realistically, all of the processes involved in RRS take a finite time to occur, such that Heisenberg's uncertainty principle restricts the accuracy to which the energy of the excited states is determined. This leads to the addition of a damping factor of $i\gamma$ in the denominator, which is inversely proportional to the lifetime of the intermediate excited states [16]. This damping factor effectively limits the maximum value of the cross-section, while broadening the resonance profile.

3.1.3   Selection rules for Raman scattering

The Raman cross-section displayed in equation (3.9) will only be different from zero if certain selection rules are respected. The most obvious of these is energy conservation, that is, $E_f = E_i$. In the limit where the matter-radiation interaction is weak, and where one extra phonon in the system does not appreciably change the electronic states of the crystal – which is true for large crystals and, specifically, for SWNTs –, the final electronic state φ_f is very close to the initial state φ_i, and the energy due to the new phonon and scattered photon equals that of the incident photon ($\hbar\omega_I = \hbar\omega_S + \hbar\omega_q$), automatically satisfying energy conservation.

Momentum conservation must also be observed throughout the entire process. The maximum momentum transfer from the radiation field to the crystal occurs for backscattered light, such that $\hbar k_I + \hbar k_S = \hbar k_q$, where k_I and k_S are the wavenumbers for incident and scattered light, respectively, and k_q is the wavenumber for the scattered phonon. The maximum k_q is given by the size of the first BZ, which is π/a, where a is the crystal's lattice constant. For SWNTs, this is typically around $10^8 \mathrm{m}^{-1}$. For visible light, k_I and k_S are of the order of $10^6 \mathrm{m}^{-1}$ for visible light. Therefore, momentum conservation restricts the phonon's wavenumber to the vicinity of the center of the first BZ, since we must obey $k_q \ll \pi/a$.

Another less obvious requirement is that there must be non-zero matrix element

$\langle x|\mathcal{H}_1|y \rangle$ connecting the initial and final states. As briefly discussed in section 2.2.2, only excitonic transition of the form E_{ii} can be promoted by light polarized along the SWNT's axis, that is, only some $\langle x|\mathcal{H}_{MR}|y \rangle$ are non-zero [32, 16]. In the specific case of the RBM phonon, which is a totally symmetric phonon, similar symmetry considerations to those involved in SWNT's optical transitions restrict the non-zero $\langle x|\mathcal{H}_{ep}|y \rangle$ to those that leave the excitonic state unaltered, or that return the exciton to the original ground state – which is not very likely because of the small energy associated with the RBM phonon.

Taking these facts into account, the dominant terms of equation (3.9) for the scattering of light by one RBM phonon can be written as [23]:

$$\sigma = C \left| \sum_a \frac{\langle 0|\mathcal{H}_{MR}|a \rangle \langle a|\mathcal{H}_{ep}|a \rangle \langle a|\mathcal{H}_{MR}|0 \rangle}{(E_{\text{laser}} - E_{ii} + i\gamma)(E_{\text{laser}} - E_{ii} - \hbar\omega_{\text{RBM}} + i\gamma)} \right|^2 \tag{3.10}$$

where $|0\rangle$ is the SWNT ground state, the sum needs only extend over the bright excitonic states [23] and we assumed for simplicity that the resonance window width is the same for both intermediate states. In the case of the RBM phonon, this assumption is also justified by the fact that the resonances with the incident and scattered photons cannot be experimentally resolved, since they are very close in energy.

3.2 Matrix elements calculations

In order to proceed with the calculation of the Raman cross-section, we must write both the perturbation Hamiltonian $\mathcal{H}_1$ and the unperturbed eigenstates explicitly. In section 2.2.2, we presented methods for the calculation of a SWNT's electronic wavefunctions, and gave a brief description of how to extend the treatment to excitonic wavefunctions. Here, we show the explicit form of the perturbation Hamiltonians, which allow us to obtain the matrix elements needed in equation (3.10).

3.2.1 Matter-radiation interaction Hamiltonian

Classical electromagnetism gives us the Hamiltonian for a spinless electron in the presence of an external electromagnetic field in the Coulomb gauge ($\vec{\nabla} \cdot \vec{A} = 0$) as [16]:

$$\mathcal{H} = \left[\frac{|\vec{p}|^2}{2m} + V(\vec{r}) \right] - \frac{e}{m}\vec{p} \cdot \vec{A} + \frac{e^2|\vec{A}|^2}{2m} \tag{3.11}$$

where $\vec{p}$, m and e are the electron's momentum, mass and charge, $\vec{A}$ and $V(\vec{r})$ are the vector potential and the crystal's potential, and $\vec{A}$ points along the direction of the oscillating incident electric field. The term in brackets is simply $\mathcal{H}_0$ for an electron in the crystal. In the weak field regime, we can neglect the $|\vec{A}|^2$ term, such that the matter-radiation interaction becomes:

$$\mathcal{H}_{MR} = -\frac{e}{m}\vec{p}\cdot\vec{A} \tag{3.12}$$

We are interested in describing an interaction between matter and visible light polarized along a SWNT's axis. Since the wavelength of visible light is much larger than a SWNT's diameter, we can neglect the spacial dependence of $\vec{A}$. A gauge transformation [50] then transforms equation (3.12) into:

$$\mathcal{H}_{MR} = -\vec{D}\cdot\vec{E} \tag{3.13}$$

where $\vec{D} = e\vec{r}$ is the dipole moment of the electron and $\vec{E}$ is the electric field. This is known as the dipole approximation for matter-radiation interaction, since it also describes the interaction between a pure dipole and an electric field.

Thus, knowledge of the relevant excitonic wavefunctions allows us to obtain the matter-radiation matrix elements involved in calculating the Raman cross-section.

3.2.2 Exciton-phonon interaction Hamiltonian

A deformation of the crystal lattice caused by a vibration changes the electronic structure of a material, introducing a coupling between a crystal's electronic and vibrational states. Within the Born-Oppenheimer approximation, which considers the electronic Hamiltonian to be independent from the momentum of the nuclei, this coupling is obtained as the difference between the Hamiltonian with atoms displaced by the vibration and with atoms at their equilibrium positions. Since the electron's momentum contributes equally to both Hamiltonians, this coupling can be written simply as [16, 51]:

$$\mathcal{H}_{ep} = V_{\vec{R}_d}(\vec{r}) - V_{\vec{R}_0}(\vec{r}) \equiv \delta V(\vec{r}) \tag{3.14}$$

where $V_{\vec{R}_d}(\vec{r})$ is the potential caused by the crystal's atoms at their displaced positions and $V_{\vec{R}_0}(\vec{r})$ is the potential caused by the crystal's atoms at their equilibrium positions.

In order to progress further, we consider the potential of each carbon atom as the Kohn-Sham potential of a neutral pseudo-atom ($v(\vec{r} - \vec{R}_\ell)$) at position $\vec{R}_\ell$ [16, 51]:

$$\delta V(\vec{r}) = \sum_\ell v(\vec{r} - \vec{R}_{d,\ell}) - v(\vec{r} - \vec{R}_{0,\ell}) \tag{3.15}$$

where the sum is over all the carbon atoms one wishes to include in the approximation. If we consider only small displacements $\vec{Q}_i$, such that $\vec{R}_{d,\ell} = \vec{R}_{0,\ell} + \vec{Q}_\ell$, we get:

$$\mathcal{H}_{ep} = \delta V(\vec{r}) = -\sum_\ell \left[\vec{\nabla}_{\vec{R}_\ell} v(\vec{r} - \vec{R}_{0,\ell})\right]_{\vec{R}_{0,\ell}} \cdot \vec{Q}_\ell \tag{3.16}$$

where the gradient $\vec{\nabla}_{\vec{R}_\ell}$ operates on the coordinates of the atoms. Here, $\vec{Q}_\ell$ points along the phonon eigenvector – radially outward, in the case of the RBM phonon – and has amplitude [16]:

$$|\vec{Q}_\ell| = \sqrt{\frac{\hbar n_q}{N_C m_C \omega_q}} \tag{3.17}$$

where N_C is the total number of carbon atoms in the SWNT, m_C is the mass of each atom, n_q is the number of existing phonons and ω_q is the phonon's frequency.

Thus, $\mathcal{H}_{ep}$ can be obtained explicitly and knowledge of the relevant excitonic wavefunctions allows us to obtain the exciton-phonon matrix elements involved in calculating the Raman cross-section.

3.2.3   Resonance window width

The resonance window width is determined by the lifetime of the intermediate states in equation (3.10). The lifetime, or its so-called relaxation time τ, is related to the resonance window width γ by the uncertainty principle as[16]:

$$\gamma = \frac{\hbar}{\tau} \tag{3.18}$$

In order to calculate the lifetime of a given state, we must consider all available scattering processes. However, the main scattering event for photoexcited electrons in SWNTs is phonon scattering [16], for which we have already obtained the interaction Hamiltonian in section 3.2.2. In the case of metallic SWNTs, plasmon scattering is also expected to be a relevant process and is treated qualitatively by Park *et al.* in [22].

Even by restricting ourselves only to electron-phonon scattering, we must still consider both the creation and absorption of any phonon mode, which can scatter the electron to any available electronic state. Our calculations are reduced by requiring energy and momentum conservations, as well as by the fact that the symmetries of the electronic states and the electron-phonon interaction restricts the allowed scattering processes. The electron-phonon interaction contribution to the resonance window width is given by [16]:

$$
\gamma = \frac{S\hbar}{8\pi m_C d_t} \sum_{\mu',k',q} \frac{\left|\langle\varphi_{\mu'}(k')|\mathcal{H}_{ep}|\varphi_\mu(k)\rangle\right|^2}{\hbar\omega_q(k'-k)} \left[\frac{dE_{\mu'}(k')}{dk'}\right]^{-1} \times
$$
$$
\times \left\{ \frac{\delta\big(E_{\mu'}(k') - E_\mu(k) - \hbar\omega_q(k'-k)\big)}{e^{\hbar\omega_q(k'-k)/k_{\mathrm{B}}T} - 1} + \right.
$$
$$
\left. + \frac{\delta\big(E_{\mu'}(k') - E_\mu(k) + \hbar\omega_q(k'-k)\big)}{1 - e^{\hbar\omega_q(k'-k)/k_{\mathrm{B}}T}} \right\} \tag{3.19}
$$

where S is the area of the graphene unit cell, m_C is the mass of a carbon atom, d_t is the SWNT diameter, $|\varphi_\mu(k)\rangle(|\varphi_{\mu'}(k')\rangle$ is the initial (scattered) electronic state, denoted by the band index $\mu(\mu')$ and wavenumber $k(k')$ and q is the phonon mode. The terms in curly brackets account for energy conservation in the creation or absorption of a phonon with wavenumber $(k'-k)$ and energy $\hbar\omega_q(k'-k)$.

Chapter 4

Experimental details

4.1 Sample selection and preparation

The SWNT sample chosen for this study was produced by water-assisted chemical vapor deposition (CVD) ("super-growth") [31], yielding a millimeter-long vertical forest of nearly isolated, high quality SWNTs [20, 28, 29, 30, 31]. Its wide d_t distribution – 1nm to 6nm, as established by high resolution transmission electron microscopy (HRTEM) [52] – along with its high quality SWNTs make this an ideal sample for a calibration of its RBM Raman intensity. The electronic and vibrational characteristics of this sample, as determined by several RRS measurements [20, 29, 30], are close to those expected from ideal free-standing, isolated SWNTs. In particular, it shows the highest E_{ii} reported in the literature and a strict adherence to the relation $\omega_{\mathrm{RBM}} = 227/d_t \, \mathrm{nm} \cdot \mathrm{cm}^{-1}$, indicating negligible environmental influence on the SWNTs' behavior.

In order for us to obtain a consistent calibration of the Raman cross-section, the same "super-growth" sample was used for both HRTEM and RRS measurements, but due to the different requirements of the techniques, were prepared in different ways. Raman measurements were performed on the as-grown sample, requiring no special sample preparation. As-grown, the "super-growth" SWNT sample is a carpet-like vertical forest of nearly vertically aligned, mostly isolated SWNTs, supported on a silicon wafer, as shown in figure 4.1 [31].

For HRTEM measurements, the sample was prepared by placing several very small
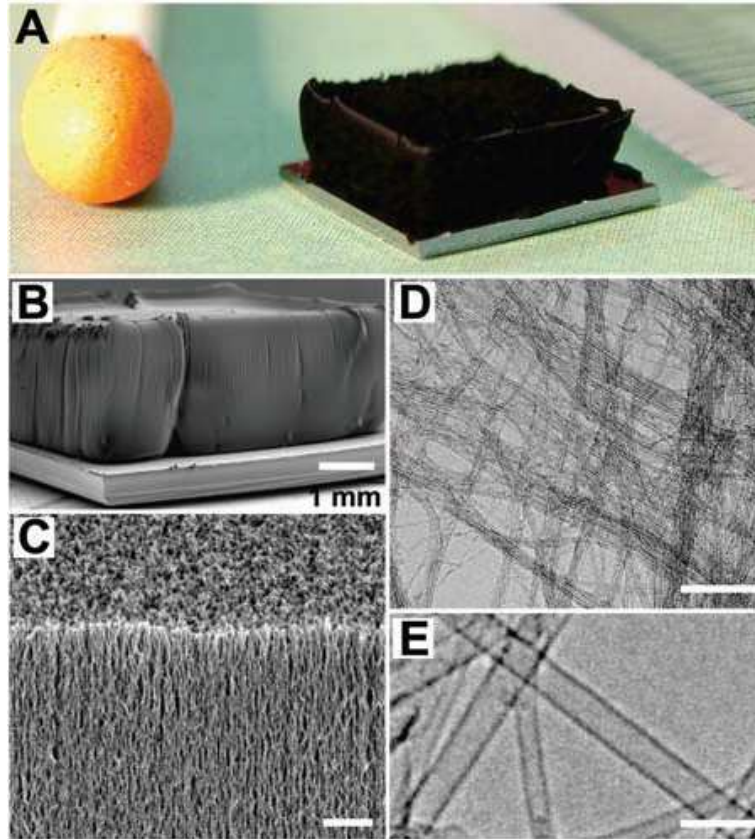
Figure 4.1: SWNT forest grown with water-assisted CVD. (A) Picture of a 2.5mm tall SWNT forest on a 7mm by 7mm silicon wafer. A matchstick on the left and ruler with millimeter markings on the right are for size reference. (B) Scanning electron microscopy image of the same SWNT forest. Scale bar, 1 mm. (C) SEM image of the SWNT forest ledge. Scale bar, 1 μm. (D) Low-resolution transmission electron microscopy image of the nanotubes. Scale bar, 100 nm. (E) HRTEM image of the SWNTs. Scale bar, 5 nm. From [31].

particles of dry, as-grown carbon nanotubes on a holey carbon TEM grid (EMS 200 mesh copper grid) supported on a piece of tissue, and wetted with a drop of methanol [53, 54]. The sample particles become compressed as the solvent evaporates, and adhere to the support film. In the process, SWNTs at the particles' extremities fold onto themselves and create loops, some of which end up being positioned normal to the grid plane. This way, it is possible to image the cross-sections of the SWNTs, represented as circles in figure 4.2(a), which facilitates diameter measurements.
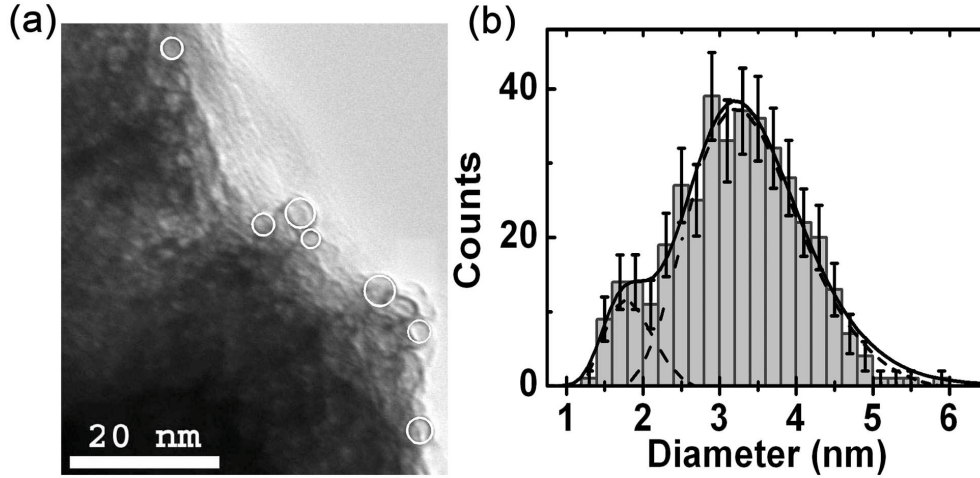
Figure 4.2: (a) HRTEM image of the SWNT sample. The white circles represent circular fittings to determine the d_t. (b) Diameter distribution of the SWNT sample measured from HRTEM images, with a binning of 0.2nm. The solid line is the sum of two log-normal distributions, represented as dashed lines, plus a small upshift, for clarity.

4.2 High resolution transmission electron microscopy

HRTEM imaging was done by collaborators from NASA Johnson Space Center, USA, using a JEOL 2000 FX instrument equipped with a LaB_6 gun, operating at a 160kV acceleration voltage and low enough beam intensity so that no irradiation damage was caused to the sample [53, 54]. Images were recorded with a 4 Megapixel Gatan CCD at a ×250,000 magnification.

Since we required accurate measurement of the SWNT diameters, and incorrect calibration of the HRTEM magnification is the largest source of systematic error, great care was taken to verify the magnification factor at ×250,000. Magnification factors were calibrated at ×600,000 and above by imaging gold crystals and determining the gold lattice parameters via their images' Fourier transforms. Then, down to ×400,000 by comparison to the graphite lattice spacing imaged at subsequently lower magnifications, and down to ×250,000 by comparison of the dimensions of multi-wall carbon nanotubes imaged at subsequently lower magnifications. In this way, a good gold lattice-based calibration was established and propagated towards lower magnifications. The calibration at ×250,000 deviated from the factory setting by only 1.5%, and was deemed satisfactory and accurate to within ±1.5%.

Homemade software developed by our collaborators from NASA was used to super-impose circles onto HRTEM images, adjust their diameters and positions until the best fit was achieved and the diameter was then determined. The accuracy of the fitting was estimated to be 0.08nm by repeatedly measuring several nanotubes and observing the spread of the determined diameters. The white circles in figure 4.2(a) are the best fits for seven SWNTs present in this image. Nanotubes with non-circular cross-sections were excluded from the analysis. The diameters of 395 different SWNTs were determined in this fashion, yielding the experimental d_t distribution seen in figure 4.2(b), obtained by binning the measured d_t in 0.2nm intervals. Error bars are determined as the standard deviation of a binomial distribution (SD = $\sqrt{Np(1-p)}$), where $N = 395$ is the sample size and p is the probability of finding a SWNT with a d_t that falls within the range of each bin. The experimentally determined diameter distribution was fitted as the sum of two log-normal distributions [55] defined as:

$$f_i = \frac{A_i}{d_t \sigma_i} \exp\left(-\frac{\ln^2(d_t/\bar{d}_i)}{2\sigma_i^2}\right) \tag{4.1}$$

where $A_1(A_2) = 4(28)$, $\bar{d}_1(\bar{d}_2) = 1.84(3.38)$nm, $\sigma_1(\sigma_2) = 0.183(0.223)$ are the parameters obtained from the fitting.

4.3   Raman spectroscopy

Raman spectra of the sample were obtained with 51 closely spaced laser lines over the 1.28eV to 1.73eV energy range, with a Ti:Sapphire laser and a SPEX triple monochromator Raman spectrometer by collaborators from the Chemistry Division of Los Alamos National Laboratory, USA. Laser power densities were kept constant and low enough (25mW with a 10cm focal distance objective) to avoid heating effects.

The Raman spectrum of a standard tylenol sample was measured after each RBM measurement, under the same laser power and focus conditions, and was used for intensity calibration of the RBM spectra. For each laser line, the non-resonant, integrated intensity of the two tylenol Raman peaks at 151cm^{-1} and 213cm^{-1} were used as intensity standards for the SWNT spectrum taken with the same laser excitation energy. In this way, the Raman intensity dependence on the constant C from equation (3.10), as well as the instrument response were accounted for, allowing us to accurately track the evolution of the sample's Raman signal over the available energy range.
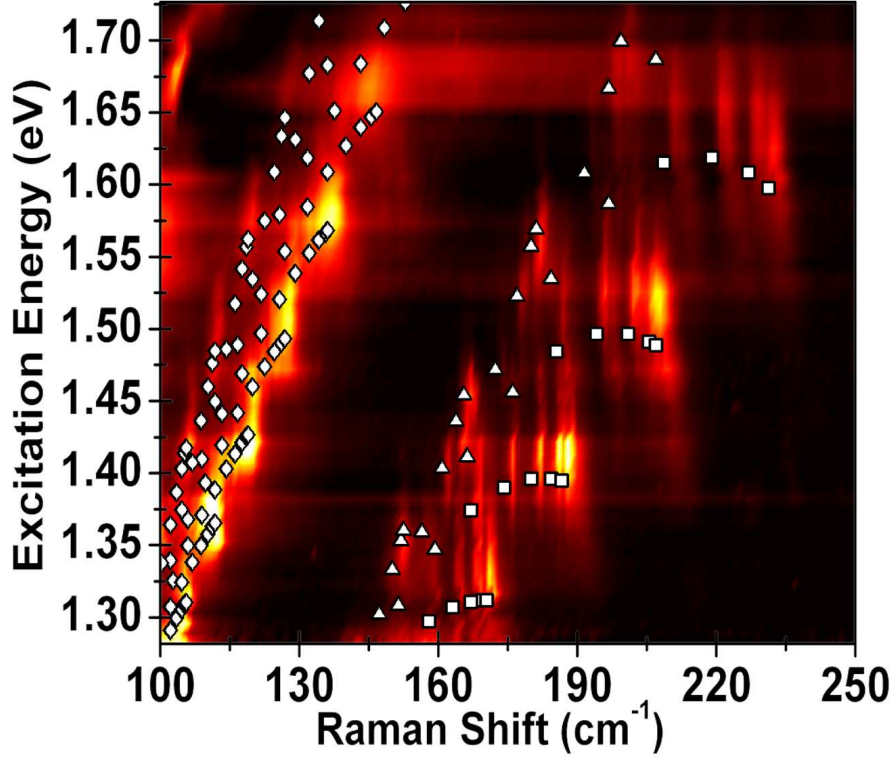
Figure 4.3: Experimentally obtained intensity-calibrated RBM RRS map. Intensity calibration was made by measuring a standard tylenol sample at each laser line. Symbols indicate the transition energies and ω_{RBM} for different SWNTs: diamonds for E_{11}^{M}, squares for $E_{22}^{\mathrm{S}_1}$ and triangles for $E_{22}^{\mathrm{S}_2}$. Brighter colors indicate higher Raman intensity. Transition energy values were obtained with equation (2.18) and the parameters from [29].

The intensity-calibrated RBM RRS map is shown in figure 4.3, along with symbols indicating the optical transition energies and ω_{RBM} for experimentally observed SWNTs: diamonds represent E_{11}^{M}, squares represent $E_{22}^{\mathrm{S}_1}$ and triangles represent $E_{22}^{\mathrm{S}_2}$. Transition energy values were obtained with equation (2.18) and the parameters from [29].

Chapter 5

Combining HRTEM and Raman

In possession of both the experimental diameter distribution and the intensity-calibrated RBM RRS map of the sample, we can calibrate the Raman cross-section and use this information to determine the diameter distribution of other SWNT samples. However, in order to proceed we must make some assumptions, described in the following section.

5.1   Model assumptions

5.1.1   Population model assumptions

HRTEM measurements determined the diameter distribution of the studied sample, not the relative population of each (n, m) species. Therefore, we assumed that SWNTs of different chiral angles are equally abundant for the "super-growth" process. Though the assumption of chirality-independent growth should not be rigorously true due to structural energy considerations, especially towards very small diameter tubes ($d_t < 1$nm) [56, 57], any under- (over-) estimation of the population of tubes with a certain chiral angle is compensated by an over- (under-) estimation of the RRS RBM cross-section dependence on θ. Therefore, its d_t dependence and consequent diameter distribution determination will still be correct.

Accepting this assumption, the relative population of each SWNT species must scale as the diameter distribution times $1/d_t$, since the number of different (n, m) species of a
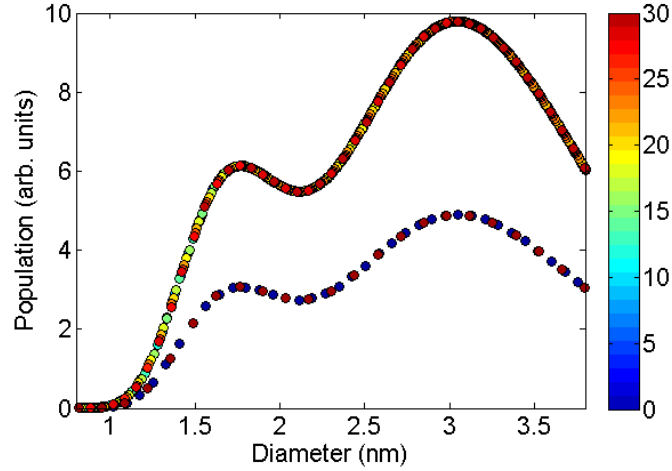
Figure 5.1: The modeled population of each nanotube species for the "super-growth" sample. The colorbar represents a species' chiral angle, in degrees. There is no need to compute the relative population of tubes with d_t greater than 4nm because their RBM frequencies fall too close to the elastically scattered laser light, below the cutoff value of our Raman spectrometer.

given diameter scales linearly with d_t. Also, chiral SWNTs ($0° < \theta < 30°$) are twice as populous as achiral ones, since both right-handed and left-handed isomers contribute to the total Raman intensity of a RBM feature assigned to an (n, m) species. The modeled (n, m) population for the "super-growth" sample is shown in figure 5.1

5.1.2 Raman cross-section model assumptions

The RBM resonance profiles obtained experimentally showed only one resonance peak, thus we were unable to separate the contributions from resonances with the incident and scattered photons. This happened because, as expected from theoretical calculations [22], the resonance window width was larger than the RBM phonon energy. Therefore, we considered the resonance window width $\gamma_{(n,m)}$ to be the same for both intermediate states.

Another constraint on experimental RRS profiles is our inability to separate the contributions to the Raman intensity originating from the matter-radiation and exciton-phonon interaction matrix elements. Therefore, the product of all matrix elements were combined into a single matrix element value $\mathcal{M}_{(n,m)}$ for each (n, m) species.

Note that, since we cannot know the absolute number of SWNTs of a given species in the spectrometer's focal region, we cannot obtain the *absolute* Raman cross-section, but rather the *relative* cross-section, which is related to the absolute cross-section by a multiplicative constant.

We modeled $\mathcal{M}_{(n,m)}$ and $\gamma_{(n,m)}$ according to the following equations:

$$\mathcal{M}_{(n,m)} = \left[\mathcal{M}_{\mathrm{A}} + \frac{\mathcal{M}_{\mathrm{B}}}{d_t} + \frac{\mathcal{M}_{\mathrm{C}}\cos(3\theta)}{d_t^2} \right]^2$$
$$\gamma_{(n,m)} = \gamma_{\mathrm{A}} + \frac{\gamma_{\mathrm{B}}}{d_t} + \frac{\gamma_{\mathrm{C}}\cos(3\theta)}{d_t^2} \tag{5.1}$$

where $\mathcal{M}_i$ and γ_i ($i =$ A,B,C) are adjustable parameters with different values for metallic, S_1 and S_2 SWNTs, since theoretical calculations [22, 23] show that the both $\gamma_{(n,m)}$ and $\mathcal{M}_{(n,m)}$ are very different depending on the SWNT's type.

These function forms were chosen because they are able to closely reproduce theoretical calculations available in the literature [22, 23], while still limiting the fitting parameters to an acceptably small number.

5.2 Simulating a resonance Raman map

Each SWNT in the sample contributes to the RBM RRS spectra with a Lorentzian lineshape [16] centered on its RBM frequency, given by:

$$L_{(n,m,\omega,E_{\mathrm{laser}})} = I_{(n,m,E_{\mathrm{laser}})} \frac{\Gamma/2}{(\omega - \omega_{\mathrm{RBM}})^2 + (\Gamma/2)^2} \tag{5.2}$$

where ω is the Raman shift, Γ is the Lorentzian's full-width at half-maximum – obtained experimentally and originating from both the spectrometer's resolution and the uncertainty in the phonon's energy – and $I_{(n,m,E_{\mathrm{laser}})}$ is its total integrated intensity at excitation laser energy E_{laser} which, once the Raman spectrum has been corrected for the spectrometer's response, is proportional to the Raman cross-section. In our study, we set $\Gamma = 3\mathrm{cm}^{-1}$, since this was the experimentally observed average for our sample. This value is in agreement with the natural FWHM for SWNT [58].

Type	$\mathcal{M}_A$	$\mathcal{M}_B$	$\mathcal{M}_C$	γ_A	γ_B	γ_C
M	1.68	0.52	5.54	23.03	48.84	1.03
S_1	-19.62	29.35	4.23	-3.45	65.10	7.22
S_2	-1.83	3.72	1.61	-10.12	42.56	-6.84

Table 5.1: Fitted parameters $\mathcal{M}_i$ and γ_i for metallic (M: $2n + m \mod 3 = 0$), semiconductor type 1 ($S_1 : 2n + m \mod 3 = 1$) and type 2 ($S_2 : 2n + m \mod 3 = 2$) SWNTs. These parameters are to be used in equation (5.1) with d_t in nm, yielding $\mathcal{M}_{(n,m)}$ in arbitrary units and $\gamma_{(n,m)}$ in meV.

From equation (3.10) and our model assumptions, we have:

$$I_{(n,m,E_{\text{laser}})} = \left| \frac{\mathcal{M}_{(n,m)}}{(E_{\text{laser}} - E_{ii} + i\gamma_{(n,m)})(E_{\text{laser}} - \hbar\omega_{\text{RBM}} - E_{ii} + i\gamma_{(n,m)})} \right|^2 \qquad (5.3)$$

$\gamma_{(n,m)}$ and $\mathcal{M}_{(n,m)}$ are described by equations (5.1) and are assumed to be constant over the observed energy range.

Since each spectrum $(S_{(\omega,E_{\text{laser}})})$ is a sum of the individual contributions of all SWNTs, it can be written as:

$$S_{(\omega,E_{\text{laser}})} = \sum_{n,m} \text{Pop}_{(n,m)} L_{(n,m,\omega)} \qquad (5.4)$$

where $\text{Pop}_{(n,m)}$ is the population of the (n,m) nanotube species.

5.3 Results

Using our models for $\text{Pop}_{(n,m)}$, $\gamma_{(n,m)}$ and $\mathcal{M}_{(n,m)}$, we simulate a RBM RRS map and adjust the fitting parameters γ_i and $\mathcal{M}_i$ in order to obtain a least squares fit to the experimental map, shown in figure 5.2(b). The best values for the fitting parameters, considering the excitonic transitions E_{22}^S and the lower branch of E_{11}^M are listed in table 5.1 for d_t in nm, $\gamma_{(n,m)}$ in meV and $\mathcal{M}_{(n,m)}$ in arbitrary units.

Figure 5.2(c) shows the absolute value of the subtraction between the experimental and modeled maps. The overall low intensity of the features in figure 5.2(c) shows that the functions chosen for $\mathcal{M}_{(n,m)}$ and $\gamma_{(n,m)}$ are representative of their experimental behavior. The most pronounced differences between the experimental and the modeled maps come from a region above E_{11}^M at around 105cm^{-1}, where there is no intensity at all on the
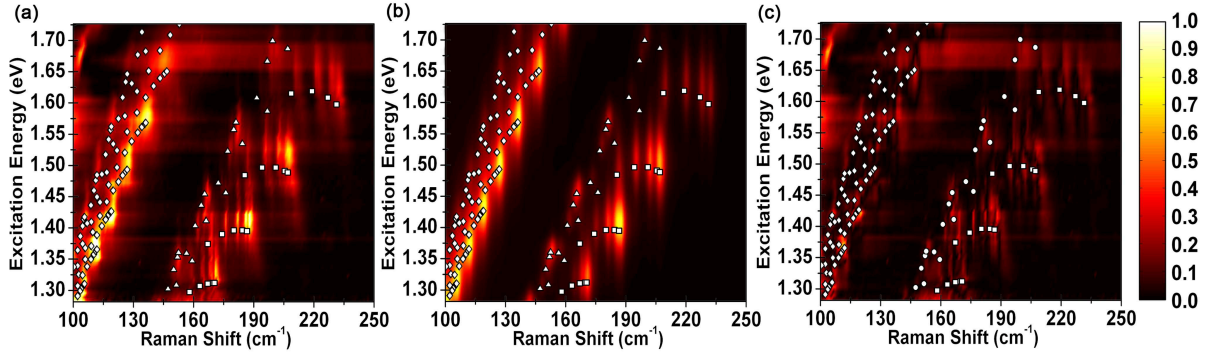
Figure 5.2: RBM RRS maps. (a) Intensity-calibrated experimental RBM RRS map. (b) Modeled RBM RRS map, obtained by using equation (5.4) with the fitting parameters in table 5.1 at the same excitation energies range as (a). (c) Absolute value of the subtraction of the experimental (a) and modeled (b) maps. Symbols indicate the transition energies and ω_{RBM} for different SWNTs: diamonds for E_{11}^{M}, squares for $E_{22}^{\text{S}_1}$ and triangles for $E_{22}^{\text{S}_2}$. The color bar scale is the same for all three maps. Transition energy values were obtained with equation (2.18) and the parameters from [29].

simulated map. This does not reflect the actual expected Raman intensity values, but is rather an artifact of the simulation: only $E_{22}^{\text{S}_1}$, $E_{22}^{\text{S}_2}$ and E_{11}^{M} resonances were simulated, while experimentally the E_{33}^{S} resonance becomes important in this region.

5.3.1 Comparison of experimental and theoretical $\mathcal{M}$ and γ

Figures 5.3(a)–(c) show a comparison of experimental and theoretical [22] values for the resonance window width $\gamma_{(n,m)}$. Additional theoretical data for metallic SWNTs with $d_t > 1.5$nm was kindly supplied by J S Park. Of note is the fact that the dependence of $\gamma_{(n,m)}$ on chiral angle is similar for both experimental and theoretical values: γ^{M} is practically independent of chiral angle, while $\gamma^{\text{S}_1}(\gamma^{\text{S}_2})$ decreases (increases) when going from zig-zag (Z) to armchair (A) SWNTs. There is very good agreement between theoretical and experimental γ^{S_2}, while there is a slight underestimation (≈ 15meV) on the theoretical calculations for γ^{S_1}. There is a larger underestimation (≈ 40meV) for γ^{M}. The underestimation of γ^{M} was already expected [22], since the theoretical calculations from the reference do not take plasmon scattering into account. One caveat is the fact that our measurements were made on an ensemble of SWNTs, each of which might be under the influence of a slightly different environment. This might lead to each SWNT having a slightly different E_{ii} transition and the sum of the contributions of all these SWNTs can
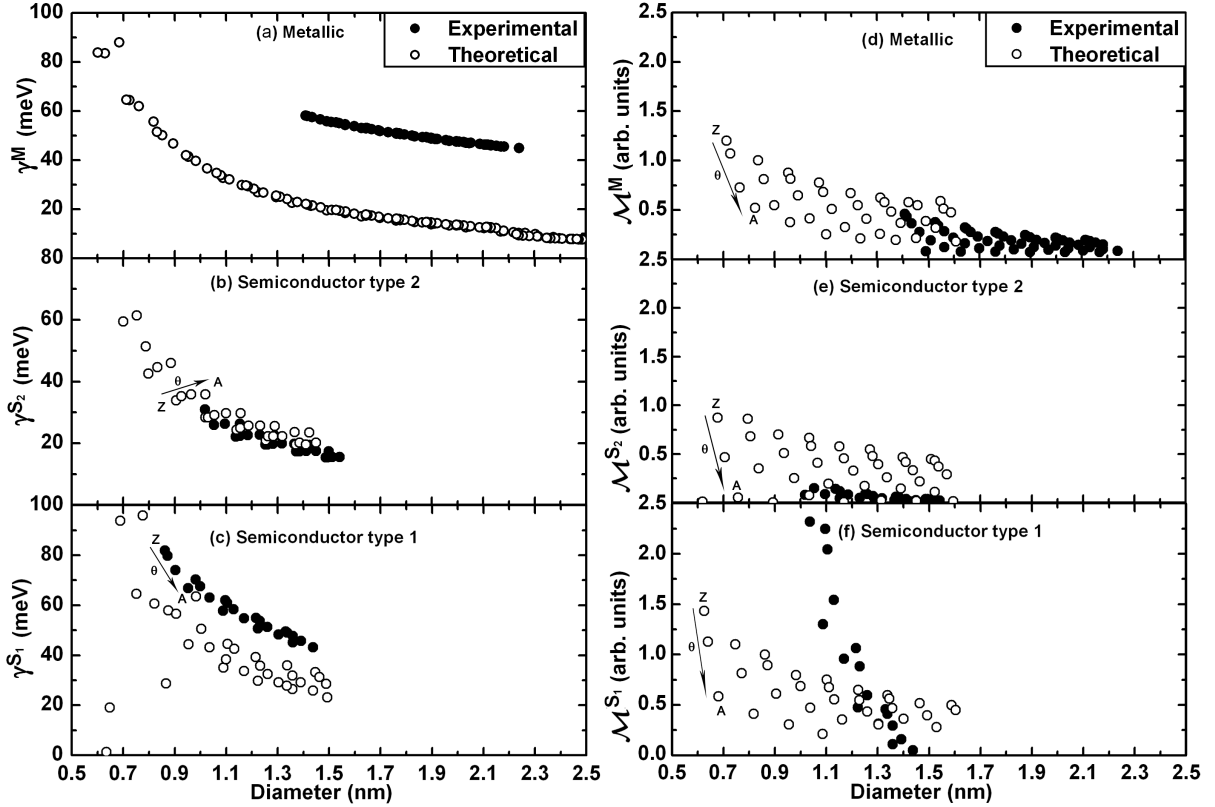
Figure 5.3: Experimental (solid circles) and theoretical (open circles) [22, 23] $\gamma_{(n,m)}$ (left) and $\mathcal{M}_{(n,m)}$ (right), separated by SWNT type (M,S$_1$,S$_2$). Values are for the E_{11}^{M} and E_{22}^{S} transitions. The letters A and Z indicate armchair-like ($\theta \approx 30°$) and zig-zag-like ($\theta \approx 0°$) SWNTs, respectively. The arrow with θ beside it indicates how the chiral angle varies within a $2n + m$ = constant family. Additional data for $d_t > 1.5$nm SWNTs was kindly supplied by J S Park. The chiral angle dependence of $\gamma_{(n,m)}$ for metallic tubes is too small to be seen here.

lead to the appearance of an enlarged $\gamma_{(n,m)}$.

Figures 5.3(d)–(f) show a comparison of experimental and theoretical [23] values for the matrix element $\mathcal{M}_{(n,m)}$. Theoretical values were obtained by the following equation:

$$\mathcal{M}_{(n,m)} = \sqrt{I_{\text{ref}} \times \left[\gamma_{\text{ref}}^2 + \left(\frac{\hbar\omega_{\text{RBM}}}{2} \right)^2 \right]} \tag{5.5}$$

where I_{ref} is the intensity per unit length, extracted from FIG.14(a) and FIG.14(c) of reference [23] and $\gamma_{\text{ref}} = 0.06\text{eV}$ is the value assumed in their paper for the resonance window width of all SWNTs. This is obtained by choosing $E_{\text{laser}} = E_{ii} + \hbar\omega_{\text{RBM}}/2$ in equation (5.3), which is the laser excitation energy for maximum RRS RBM intensity.

Consistently with the theoretical predictions, our measurements show the largest values for $\mathcal{M}^{\text{S}_1}$, while $\mathcal{M}^{\text{S}_2}$ and $\mathcal{M}^{\text{M}}$ are of the same order of magnitude. However, we find a steeper dependence of $\mathcal{M}^{\text{S}_1}$ on tube diameter than predicted by theory [23], as well as a theoretical overestimation of the chiral angle dependence of $\mathcal{M}^{\text{S}_2}$.

Chapter 6

Applications

6.1 Determining a sample's diameter distribution from Raman RBM spectra

In order to determine the diameter distribution of a SWNT sample from RBM RRS measurements alone, one needs to know the RRS RBM cross-section of each tube in the sample, which includes knowledge of E_{ii}, ω_{RBM}, $\mathcal{M}_{(n,m)}$ and $\gamma_{(n,m)}$. E_{ii} and ω_{RBM} are obtained from the literature for a wide variety of samples and a general picture has been provided for both [20, 30]. The values for $\mathcal{M}_{(n,m)}$ and $\gamma_{(n,m)}$ can be determined by using the fitting parameters provided in table 5.1 in equations (5.1) for the E_{22}^{S} and E_{11}^{M} optical transitions, under the assumptions described in section 5.1. We then compare the predicted RRS RBM intensities with the relative intensity ratios obtained from experimental RRS RBM spectra and obtain the diameter distribution of the sample.

The easiest way to compare the experimental intensities with the calculated RRS RBM cross-sections is to compare the experimental spectra with simulated spectra obtained by assuming a "dummy" constant diameter distribution, a procedure which is accomplished with the help of the MatLab program `SpectraSimulation.m` in appendix A. (**Important: this program only simulates resonance with E_{22}^{S} and E_{11}^{M}**). We assume that SWNTs with different chiral angles are equally abundant. This means that
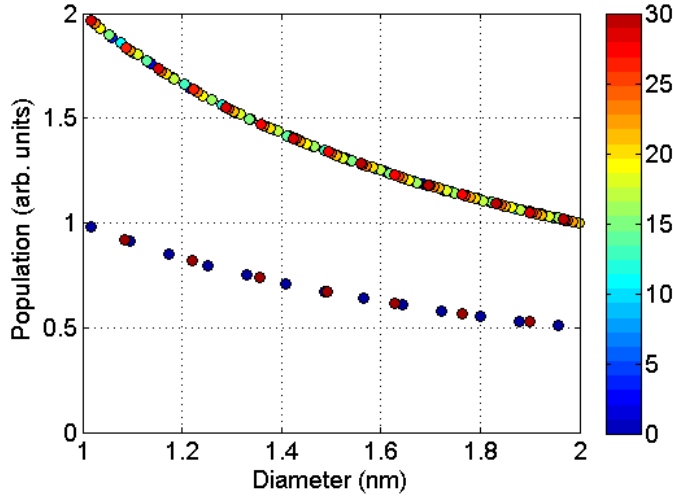
Figure 6.1: The modeled population of each nanotube species for the "dummy" population, with a constant diameter distribution. The colorbar represents a species' chiral angle, in degrees.

the population of each tube is given by:

$$\text{Pop}_{(n,m)} = \begin{cases} 1/d_t & \text{if } \theta = 0° \text{ or } \theta = 30° \\ 2/d_t & \text{otherwise} \end{cases} \tag{6.1}$$

since the density of different (n,m) species scales linearly with d_t and chiral tubes have optical isomers (right-handed and left-handed varieties both of which contribute to the same RBM feature) while achiral tubes do not. This "dummy" population is shown in figure 6.1. Using this "dummy" population, we simulate spectra using the same laser excitation energies that were used experimentally with equation (5.4).

The MatLab program `SpectraSimulation.m` in appendix A generates a spectrum using the equations and parameters described here for $\gamma_{(n,m)}$ and $\mathcal{M}_{(n,m)}$, taking only E_{22}^{S} and E_{11}^{M} resonances into account. The simulated spectrum is exported as the file `SimSpec[`E_{laser}`].txt`, where the used excitation energy substitutes the string [E_{laser}] in the file name. Parameters adequate for SWNT samples with small bundles or SWNTs wrapped in surfactants are used for E_{ii} [36] and ω_{RBM} [20]. All one needs to do is to run the program and state the E_{laser} that was used and the observed experimental full-width at half-maximum of RBM features (Γ) in cm^{-1}. Bear in mind that the parameters defined internally by the program for E_{ii} and ω_{RBM} may need to be changed, depending on the studied sample.
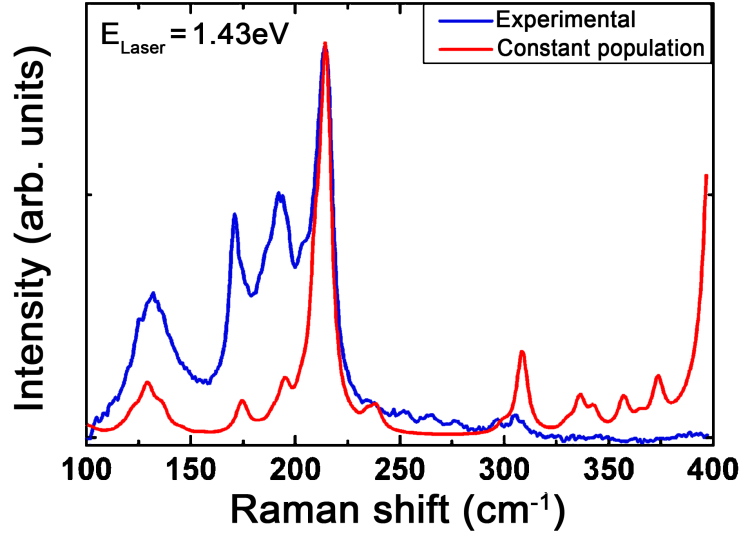
32

Figure 6.2: Experimental (blue) spectrum from an alcohol CVD SWNT sample [36] and simulated (red) spectrum, obtained by using equation 5.4 and the "dummy" constant population distribution (see text). The two spectra are normalized by a common RBM peak. As expected, the spectra do not match, since the sample's diameter distribution is not the same as the "dummy" constant diameter distribution.

Now, compare each experimental RBM spectrum with its simulated counterpart by fitting each of them with the same number of Lorentzians, each centered at the same wavenumber (allowing a freedom of $\pm 3 \mathrm{cm}^{-1}$, to account for experimental error). The ratio between the areas under these peaks will be directly proportional to the population ratio between the real sample's d_t distribution and the constant "dummy" d_t distribution. In order to transform the axis from Raman shift (cm^{-1}) into d_t (nm), all one needs is the correct $\omega_{\mathrm{RBM}} \to d_t$ relation. By default, the program uses equation (2.20) with $C = 0.05786 \mathrm{nm}^{-2}$, which is a constant that fits the data for most of the samples in the literature [20], but may need to be changed depending on your sample. Equation (2.20) can be easily inverted to yield:

$$d_t = \left[\frac{\omega^2}{A^2} - C \right]^{-1/2} \tag{6.2}$$

where $A = 227 \mathrm{nm \cdot cm}^{-1}$ [20].

Plotting the area ratios versus d_t (obtained from the Raman shift by inverting) yields the diameter distribution. Figures 6.2 and 6.3 show an illustrative example of this procedure done with a single laser line for an alcohol CVD SWNT sample [36]. Notice,
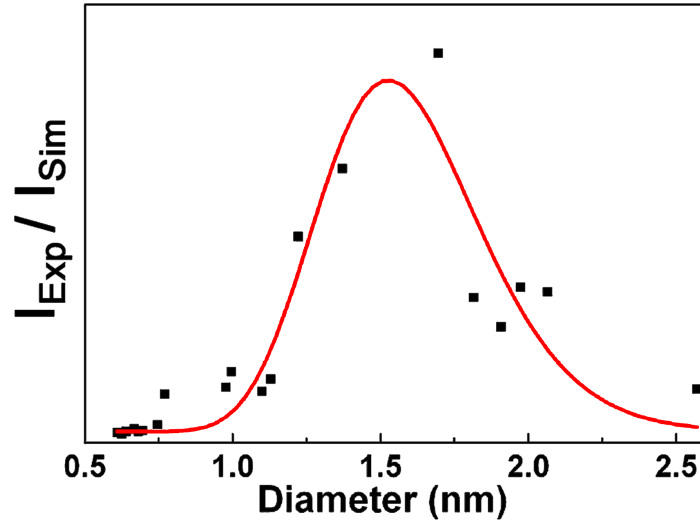
Figure 6.3: Black squares represent the integrated area ratios between the Lorentzian peaks used to fit the experimental and simulated spectra in figure 6.2. The red curve is a lognormal [55] fit to the data points. The horizontal axis was transformed from Raman shift (cm^{-1}) to diameter (nm) by using equation (6.2).

however, that only SWNTs which are resonant at the used laser excitation energy can be probed, so the use of multiple excitation energies can dramatically increase the accuracy of this procedure.

Chapter 7

Final remarks

In summary, we have combined the diameter distribution of a SWNT sample, obtained by high resolution transmission electron microscopy, and a RBM resonance Raman map in order to determine the RBM Raman cross-section of a wide variety of SWNTs. This result allows us to use a sample's RBM signal in the inverse process, that is, to determine its diameter distribution using only resonance Raman scattering. Due to the very special nature of the "super-growth" sample, the values displayed here are representative of nearly ideal SWNTs, such that the results of this study are useful as experimental data for theorists, as well as a tool which we hope will be useful to experimentalists.

While the procedure described in 6 remains assumption-dependent for a determination of the relative population of an individual (n, m) species, it is assumption-independent for obtaining the diameter distribution. Notice also that the fitting parameters $\mathcal{M}_i$ and γ_i were obtained with excitation energies between 1.26eV and 1.73eV for the water-assisted CVD "super-growth" SWNT sample, so that diameter distributions determined from RRS RBM measurements within this energy range are expected to be more accurate. It is also important to notice that the values for $\gamma_{(n,m)}$ and $\mathcal{M}_{(n,m)}$ may vary depending on the kind of sample [59] one has, so the most accurate results will be obtained for samples similar to the "super-growth" sample. This is especially true for the value of $\gamma_{(n,m)}$ for bundled SWNTs, which can be significantly larger than those of the "super-growth" sample [59], so an adequate rescaling might be necessary. An underestimation of $\gamma_{(n,m)}$ will lead to an overestimation of the population of SWNTs which are not fully resonant at the used E_{laser} (due to a decreased estimated resonance window width) and an underestimation of the

population for those SWNT which are fully resonant at E_{laser} (due to an overall increase of the estimated RRS RBM cross-section).

Despite these caveats, this procedure is an important quantitative step towards the accurate characterization of SWNT samples, facilitating their commercial use. Brazil's National Metrology Institute (INMETRO - Instituto Nacional de Metrologia, Qualidade e Tecnologia) used the methodology presented here on measurements for a recent project by the USA National Institute of Standards and Technology (NIST VAMAS TWA 34, project #1) [60], which hopes to establish the chirality distribution of a metrological reference material (RM) SWNT sample, as measured by several different laboratories, with different techniques. It is hoped that further comparison of the results of different methodologies will help refine and expand the parameters used in the population assessment of SWNT samples by resonance Raman scattering.

Appendix A

SpectraSimulation.m MatLab program

```
%IMPORTANT! This program requires a clean workspace and thus begins with a
%"clear" command. Please take the appropriate measures is you wish to save
%your workspace before running this program.
%
%This program  simulates the Raman RBM spectrum of a SWNT with a constant
%diameter distribution, as explained previously. The simulated
%spectrum is exported to the file SimSpec[E_L].txt , where the actual
%excitation energy used replaces [E_L] in the file name.
%
%The parameters we use to define the RBM frequency and transition energies
%should be valid for SWNT sample with small bundles or of SWNTs wrapped in
%surfactancts.  If your sample is very different, the parameters defined in
%the program should be changed. All of the values that might need to be
%changed are commented as such.
%
%We define the basic properties of SWNTs based on their (n,m)
%indices. MatLab conventions demand the use of indices that start with 1,
%so througout the programs the variable k=m+1 will be used whenever needed.
```

```
clear

nmin=3; %Tubes from (nmin,0) up to (nmax,nmax) will be considered
nmax=40;

C=0.05786; %This constant is used to determine the RBM of the tubes.
           %PRB 77, 241403 (2008).
%This value is adequate for bundled or wrapped SWNTs and might need to be
%changed depending on the sample you are studying.




%First we determine the basic structural properties of the tubes.
%Pre-allocating some variables, for better speed
tamn=nmin:nmax;
tamk=1:nmax+1;
d(tamn,tamk)=0;
cosa(tamn,tamk)=0;
cos3angle(tamn,tamk)=0;
fam(tamn,tamk)=NaN;
rbm(tamn,tamk)=0;
Eph(tamn,tamk)=0;
popconst(tamn,tamk)=0;

for n=nmin:nmax
    for k=1:n+1 %m starts from 0 and goes to n
        m=k-1;
        d(n,k)=0.142*(3*(n.^2+n*m+m.^2))^0.5/3.141593;
        %tube diameter in nm, using a c-c distance of 0.142 nm

        cosa(n,k)=(2*n+m)./(2*((n.^2+n*m+m.^2)^0.5));
        cos3angle(n,k)=cos(3*acos(cosa(n,k))); %cos(3*theta)
        fam(n,k)=mod((2*n+m),3);
        %tube type. 0=> metallic ;  1=> S_1 ; 2=> S_2
```

```matlab
        rbm(n,k)=227/d(n,k)*sqrt(1+C*d(n,k)^2);
        %SWNT's RBM frequency, in cm^-1.PRB 77, 241403 (2008).


        Eph(n,k)=(1.239842E-4)*rbm(n,k);
        %hbar*wRBM. Energy of the RBM phonon in eV


        if k==1 || k==n+1 %if the tube is achiral
            popconst(n,k)=1/d(n,k);
            %This population is for the "dummy" diameter distribution
        else %if the tube is chiral
            popconst(n,k)=2/d(n,k);
            %If the tube is chiral, then left- and right-handed isomers
            %contribute
        end


    end
end


%Now we determine their transition energies. These values were taken from
%PRL 98, 067401 (2007) and should be valid for samples consisting of small
%bundles or of SWNTs wrapped with surfactants. For freestanding
%individualized SWNTs (such as those in the "super-growth" sample), the
%values of Phys. Stat. Sol. (b) 245, No. 10, 2201-2204 (2008)
%/ DOI 10.1002/pssb.200879625 should be used.

%These values might need to be changed depending on your sample. Please see
%PRL 103, 146802 (2009) for a discussion on how the environment can change
%the transition energies of tubes.

%The following values are for Eii in units of eV and d(n,k) in nm.
Elin=1.049;
Elog=0.456;
lambda=0.812;
g=0.305;
```

39

```matlab
%Eii S1
betas(1,1)= 0.05; %E11
betas(1,2)=-0.19; %E22
betas(1,4)= 0.42; %E33
betas(1,5)=-0.4; %E44


%Eii S2
betas(2,1)=-0.07; %E11
betas(2,2)= 0.14; %E22
betas(2,4)=-0.42; %E33
betas(2,5)= 0.4; %E44


%Eii M
betam(1,1)=0.19; %E11M upper branch. Not usually observed in Raman
betam(1,2)=-0.19; %E11M lower branch


%Now we calculate the transition energies in units of eV

%First we pre-allocate for speed
tamp=1:4;
TE(tamp,tamn,tamk)=0;


for n=nmin:nmax
    for k=1:n+1

        %S2 semiconducting nanotubes transition energies
        if fam(n,k)==2
            TE(1,n,k)=  Elin*1/d(n,k).*(1+Elog*log10(lambda*d(n,k)./1))+...
                        betas(2,1)*cos3angle(n,k)./(d(n,k).^2); %E11 S2
            TE(2,n,k)=  Elin*2/d(n,k).*(1+Elog*log10(lambda*d(n,k)./2))+...
                        betas(2,2)*cos3angle(n,k)./(d(n,k).^2); %E22 S2
            TE(3,n,k)=  Elin*4/d(n,k).*(1+Elog*log10(lambda*d(n,k)./4))+...
                        betas(2,4)*cos3angle(n,k)./(d(n,k).^2)+g/(d(n,k));
                        %E33 S2
```

```
        TE(4,n,k)=  Elin*5/d(n,k).*(1+Elog*log10(lambda*d(n,k)./5))+...
                    betas(2,5)*cos3angle(n,k)./(d(n,k).^2)+5/4*...
                    g/(d(n,k)); %E44 S2

    end


    %S1 semiconducting nanotubes transition energies
    if fam(n,k)==1
        TE(1,n,k)=  Elin*1/d(n,k).*(1+Elog*log10(lambda*d(n,k)./1))+...
                    betas(1,1)*cos3angle(n,k)./(d(n,k).^2); %E11 S1
        TE(2,n,k)=  Elin*2/d(n,k).*(1+Elog*log10(lambda*d(n,k)./2))+...
                    betas(1,2)*cos3angle(n,k)./(d(n,k).^2); %E22 S1
        TE(3,n,k)=  Elin*4/d(n,k).*(1+Elog*log10(lambda*d(n,k)./4))+...
                    betas(1,4)*cos3angle(n,k)./(d(n,k).^2)+g/(d(n,k));
                    %E33 S1


        TE(4,n,k)=  Elin*5/d(n,k).*(1+Elog*log10(lambda*d(n,k)./5))+...
                    betas(1,5)*cos3angle(n,k)./(d(n,k).^2)+5/4*...
                    g/(d(n,k)); %E44 S1

    end


    %M metallic nanotubes
    if fam(n,k)==0
        TE(1,n,k)=  Elin*3./d(n,k).*(1+Elog*log10(lambda*d(n,k)./3))...
                    +betam(1,1)*cos3angle(n,k)./d(n,k).^2;
                    %E11M upper branch


        TE(2,n,k)=  Elin*3./d(n,k).*(1+Elog*log10(lambda*d(n,k)./3))...
                    +betam(1,2)*cos3angle(n,k)./d(n,k).^2;
                    %E11M lower branch
    end
end
end
```

41

```
%Now we determine the Raman properties of the tubes, based on the values
%from our paper. These are only valid for E22^S and E11^M (lower branch).

%Parameters for the matrix element
aMS1=[-19.62 29.35 4.23]';
aMS2=[ -1.83  3.72 1.61]';
aMM =[  1.68  0.52 5.54]';

%Parameters for the resonance window width gamma
aGS1=[ -3.45 65.10  7.22]';
aGS2=[-10.12 42.56 -6.84]';
aGM =[ 23.03 48.84  1.03]';

%First we pre-allocate for speed
M(tamn,tamk)=0;
G(tamn,tamk)=0;

for n=nmin:nmax
    for k=1:n+1
        if fam(n,k)==1 %For S1 tubes
            M(n,k)=([1 1/d(n,k) cos3angle(n,k)/d(n,k)^2]*aMS1)^2;
            G(n,k)=[1 1/d(n,k) cos3angle(n,k)/d(n,k)^2]*aGS1*10^-3;
            %the 10^-3 factor is so the values are in eV, not in meV
        elseif fam(n,k)==2 %For S2 tubes
            M(n,k)=([1 1/d(n,k) cos3angle(n,k)/d(n,k)^2]*aMS2)^2;
            G(n,k)=[1 1/d(n,k) cos3angle(n,k)/d(n,k)^2]*aGS2*10^-3;
            %the 10^-3 factor is so the values are in eV, not in meV
        elseif fam(n,k)==0 %For metallic tubes
            M(n,k)=([1 1/d(n,k) cos3angle(n,k)/d(n,k)^2]*aMM)^2;
            G(n,k)=[1 1/d(n,k) cos3angle(n,k)/d(n,k)^2]*aGM*10^-3;
            %the 10^-3 factor is so the values are in eV, not in meV
        end
    end
```

```matlab
end

%Now all we need is to calculate the expected spectrum of this "dummy" SWNT
%population

w=10:550; %this is the frequency range of the Raman spectrum in cm^-1.
          %Feel free to change this according to your preference

EL=input('Excitation energy in eV = '); %This is the laser excitation
%energy used in eV. This should be changed acording to the laser
%excitation energy you used for the experimental spectrum.

FW=input('FWHM for the RBM Lorentzian in cm^-1 = '); %This is the
%Full-Width at Half-Maximum intensity (in cm^-1) for the tube's RBM
%lorentzian. This should be changed to match the values you get for your
%sample.

S(1:max(size(w)))=0; %The spectrum starts as a baseline, at 0 intensity.

%First we pre-allocate for speed
I(tamn,tamk)=0;

for n=nmin:nmax
    for k=1:n+1

        I(n,k)= (abs(M(n,k)/((EL-TE(2,n,k)+1i*G(n,k))*(EL-TE(2,n,k)-...
                Eph(n,k)+1i*G(n,k)))))^2;

        for cont=1:max(size(w))
            S(cont)=S(cont) + popconst(n,k)*I(n,k)*(FW/2)/((w(cont)-...
                    rbm(n,k))^2+(FW/2)^2);
        end
    end
end
```

```
dlmwrite(['SimSpec' num2str(EL) '.txt'], [w' S'],' ')

figure(1)
plot(w,S,'k-')
title(['Simulated spectrum at ' num2str(EL) 'eV'])
xlabel('Raman shift (cm^-^1)')
ylabel('Raman intensity (arb. units)')
```

Bibliography

[1] S.B. Mitra, D. Wu, and B.N. Holmes. An application of nanotechnology in advanced dental materials. *The Journal of the American Dental Association*, 134(10):1382, 2003.

[2] D. Pum and U.B. Sleytr. The application of bacterial s-layers in molecular nanotechnology. *Trends in Biotechnology*, 17(1):8–12, 1999.

[3] L.S. Zhong, J.S. Hu, A.M. Cao, Q. Liu, W.G. Song, and L.J. Wan. 3d flowerlike ceria micro/nanocomposite structure and its application for water treatment and co removal. *Chemistry of Materials*, 19(7):1648–1655, 2007.

[4] D.K. Tiwari, J. Behari, and P. Sen. Application of nanoparticles in waste water treatment. *Carbon Nanotubes*, 3(3):417–433, 2008.

[5] P. Guo. Rna nanotechnology: engineering, assembly and applications in detection, gene delivery and therapy. *Journal of nanoscience and nanotechnology*, 5(12):1964, 2005.

[6] J. Shi, A.R. Votruba, O.C. Farokhzad, and R. Langer. Nanotechnology in drug delivery and tissue engineering: From discovery to applications. *Nano letters*, 2010.

[7] E. Frackowiak and F. Beguin. Electrochemical storage of energy in carbon nanotubes and nanostructured carbons. *Carbon*, 40(10):1775–1787, 2002.

[8] M. Terrones, F. Banhart, N. Grobert, J.C. Charlier, H. Terrones, and PM Ajayan. Molecular junctions by joining single-walled carbon nanotubes. *Physical review letters*, 89(7):75505, 2002.

[9] S.J. Tans, A.R.M. Verschueren, and C. Dekker. Room-temperature transistor based on a single carbon nanotube. *Nature*, 393(6680):49–52, 1998.

[10] R. Martel, T. Schmidt, HR Shea, T. Hertel, and P. Avouris. Single-and multi-wall carbon nanotube field-effect transistors. *Applied Physics Letters*, 73:2447, 1998.

[11] A. Star, V. Joshi, S. Skarupo, D. Thomas, and J.C.P. Gabriel. Gas sensor array based on metal-decorated carbon nanotubes. *The Journal of Physical Chemistry B*, 110(42):21014–21020, 2006.

[12] A.K.T. Lau and D. Hui. The revolutionary creation of new advanced materials carbon nanotube composites. *Composites Part B: Engineering*, 33(4):263–277, 2002.

[13] D. Tománek and R.J. Enbody. *Science and application of nanotubes*. Springer, 2000.

[14] V.N. Popov. Carbon nanotubes: properties and application. *Materials Science and Engineering: R: Reports*, 43(3):61–102, 2004.

[15] G. Dresselhaus R. Saito and M. S. Dresselhaus. *Physical Properties of Carbon Nanotubes*. Imperial College Press, London, 1998.

[16] R. Saito A. Jorio, M. S. Dresselhaus and G. Dresselhaus. *Raman Spectroscopy in Graphene Related Systems*. WILEY-VCH, Weinheim, 2011.

[17] Z. Luo, L.D. Pfefferle, G.L. Haller, and F. Papadimitrakopoulos. (n, m) abundance evaluation of single-walled carbon nanotubes by fluorescence and absorption spectroscopy. *Journal of the American Chemical Society*, 128(48):15511–15516, 2006.

[18] Z. Luo, F. Papadimitrakopoulos, and S.K. Doorn. Bundling effects on the intensities of second-order raman modes in semiconducting single-walled carbon nanotubes. *Physical Review B*, 77(3):035421, 2008.

[19] A. Jorio, R. Saito, J. H. Hafner, C. M. Lieber, M. Hunter, T. McClure, G. Dresselhaus, M. S. Dresselhaus,. *Physical Review Letters*, 86:1118, 2001.

[20] P. T. Araujo, I. O. Maciel, P. B. C. Pesce, M. A. Pimenta, S. K. Doorn, H. Qian, A. Hartschuh, M. Steiner, L. Grigorian, K. Hata, A. Jorio. Nature of the constant factor in the relation between radial breathing mode frequency and tube diameter for single-wall carbon nanotubes. *Physical Review B*, 77:241403(R), 2008.

[21] A. Jorio, C. Fantini, M. A. Pimenta, R. B. Capaz, Ge. G. Samsonidze, G. Dresselhaus, M. S. Dresselhaus, J. Jiang, N. Kobayashi, A. Grüneis, R. Saito,. *Physical Review B*, 71:075401, 2005.

[22] JS Park, Y. Oyama, R. Saito, W. Izumida, J. Jiang, K. Sato, C. Fantini, A. Jorio, G. Dresselhaus, and MS Dresselhaus. Raman resonance window of single-wall carbon nanotubes. *Physical Review B*, 74(16):165414, 2006.

[23] J. Jiang, R. Saito, K. Sato, JS Park, G.G. Samsonidze, A. Jorio, G. Dresselhaus, and MS Dresselhaus. Exciton-photon, exciton-phonon matrix elements, and resonant raman intensity of single-wall carbon nanotubes. *Physical Review B*, 75(3):035405, 2007.

[24] M. Machón, S. Reich, H. Telg, J. Maultzsch, P. Ordejon, C. Thomsen. *Physical Review B*, 71:035416, 2005.

[25] T. Okazaki, T. Saito, K. Matsuura, S. Ohshima, M. Yumura, Y. Oyama, R. Saito, and S. Iijima. Photoluminescence and population analysis of single-walled carbon nanotubes produced by cvd and pulsed-laser vaporization methods. *Chemical physics letters*, 420(4-6):286–290, 2006.

[26] A. Jorio, AP Santos, HB Ribeiro, C. Fantini, M. Souza, JPM Vieira, CA Furtado, J. Jiang, R. Saito, L. Balzano, et al. Quantifying carbon-nanotube species with resonance raman scattering. *Physical Review B*, 72(7):075207, 2005.

[27] H. Telg, J. Maultzsch, S. Reich, and C. Thomsen. Resonant-raman intensities and transition energies of the e_- {11} transition in carbon nanotubes. *Physical Review B*, 74(11):115415, 2006.

[28] S. K. Doorn, P. T. Araujo, K. Hata, A. Jorio. *Physical Review B*, 78:165408, 2008.

[29] P. T. Araujo and A. Jorio. *Physica Status Solid (b)*, 245:2201, 2008.

[30] P. T. Araujo, A. Jorio, M. S. Dresselhaus, K. Sato, R. Saito. *Physical Review Letters*, 103:146802, 2009.

[31] K. Hata, D. N. Futaba, K. Mizuno, T. Namai, M. Yumura, S. Iijima,. *Science*, 306:1362, 2004.

[32] E.B. Barros, A. Jorio, G.G. Samsonidze, R.B. Capaz, A.G. Souza Filho, J. Mendes Filho, G. Dresselhaus, and M.S. Dresselhaus. Review on the symmetry-related properties of carbon nanotubes. *Physics reports*, 431(6):261–302, 2006.

[33] C. F. Leite. *Estudo de Propriedades Eletrônicas e Vibracionais de Nanotubos de Carbono por Espalhamento Raman Ressonante*. Department of Physics - Federal University of Minas Gerais, 2006.

[34] P. A. Araujo. *Study of the Electrostatic Shielding and Environmental Interactions in Carbon Nanotubes by Resonance Raman Spectroscopy*. Department of Physics - Federal University of Minas Gerais, 2010.

[35] M.S. Dresselhaus, G. Dresselhaus, R. Saito, A. Jorio. *Physics Reports*, 409:47, 2004.

[36] P. T. Araujo, S. K. Doorn, S. Kilina, S. Tretiak, E. Einarsson, S. Maruyama, H. Chacham, M. A. Pimenta, A. Jorio,. *Physical Review Letters*, 98:067401, 2007.

[37] V. N. Popov. *New Journal of Physics*, 6:17, 2004.

[38] Ge. G. Samsonidze, R. Saito, N. Kobayashi, A. Grüneis, J. Jiang, A. Jorio, S. G. Chou, G. Dresselhaus, M. S. Dresselhaus. *Applied Physics Letters*, 85:5703, 2004.

[39] F. Wang, G. Dukovic, L. E. Brus, T. F. Heinz,. *Science*, 308:838, 2005.

[40] J. Maultzsch, R. Pomraenke, S. Reich, E. Chang, D. Prezzi, A. Ruini, E. Molinari, M. S. Strano, C. Thomsen, C. Lienau. *Physical Review B*, 72:241402(R), 2005.

[41] J. Jiang, R. Saito, G.G. Samsonidze, A. Jorio, SG Chou, G. Dresselhaus, and M.S. Dresselhaus. Chirality dependence of exciton effects in single-wall carbon nanotubes: Tight-binding model. *Physical Review B*, 75(3):035407, 2007.

[42] M.S. Dresselhaus, G. Dresselhaus, R. Saito, and A. Jorio. Exciton photophysics of carbon nanotubes. *Annu. Rev. Phys. Chem.*, 58:719–747, 2007.

[43] C. L. Kane and E. J. Mele. *Physical Review Letters*, 90:207401, 2003.

[44] C. L. Kane and E. J. Mele. *Physical Review Letters*, 93:197402, 2004.

[45] M. J. Longhurst, N. Quirke,. *Journal of Chemical Physics*, 124:234708, 2006.

[46] G. D. Mahan,. *Physical Review B*, 65:235402, 2002.

[47] L. G. Cancado. *Raman Spectroscopy of Nanographites*. Department of Physics - Federal University of Minas Gerais, 2006.

[48] R. M. Martin and L. M. Falicov. *Light-Scattering in Solids*. Springer-Verlag, Berlin, 1975.

[49] L. M. Guimaraes. *Perfis de espalhamento Raman ressonante em estruturas unidimensionais de carbono: cadeias lineares e nanotubos quiralmente enriquecidos*. Department of Physics - Federal University of Minas Gerais, 2011.

[50] Diu Cohen-Tannoudji and Laloe. *Quantum Mechanics, vol 2*. Hermann and John Wiley& Sons, 1977.

[51] J. Jiang, R. Saito, Ge. G. Samsonidze, S. G. Chou, A. Jorio, G. Dresselhaus, M. S. Dresselhaus. *Physical Review B*, 72:235408, 2005.

[52] P B. C. Pesce, P. T. Araujo, P. Nikolaev, S. K. Doorn, K. Hata, R. Saito, M. S. Dresselhaus, A. Jorio. *Applied Physics Letters*, 96:051910, 2010.

[53] A. Thess, R. Lee, P. Nikolaev, H. Dai, P. Petit, J. Robert, C. Xu, Y.H. Lee, S.G. Kim, A.G. Rinzler, et al. Crystalline ropes of metallic carbon nanotubes. *Science*, 273(5274):483, 1996.

[54] P. Nikolaev, A. Thess, A.G. Rinzler, D.T. Colbert, and R.E. Smalley. Diameter doubling of single-wall nanotubes. *Chemical physics letters*, 266(5-6):422–426, 1997.

[55] LB Kiss, J. Söderlund, GA Niklasson, and CG Granqvist. New approach to the origin of lognormal size distributions of nanoparticles. *Nanotechnology*, 10:25, 1999.

[56] D.A. Gómez-Gualdrón and P.B. Balbuena. The role of cap chirality in the mechanism of growth of single-wall carbon nanotubes. *Nanotechnology*, 19:485604, 2008.

[57] S. Reich, L. Li, and J. Robertson. Structure and formation energy of carbon nanotube caps. *Physical Review B*, 72(16):165423, 2005.

[58] A. Jorio, C. Fantini, MSS Dantas, MA Pimenta, AG Souza Filho, G.G. Samsonidze, VW Brar, G. Dresselhaus, MS Dresselhaus, AK Swan, et al. Linewidth of the raman features of individual single-wall carbon nanotubes. *Physical Review B*, 66(11):115411, 2002.

[59] Z. Luo, F. Papadimitrakopoulos, and S.K. Doorn. Bundling effects on the intensities of second-order raman modes in semiconducting single-walled carbon nanotubes. *Physical Review B*, 77(3):035421, 2008.

[60] Erlon Ferreira. Resonance Raman RBM Intensity Analysis of the NIST Sample RM 8281 Long Fraction, 2010. http://www.nist.gov/mml/polymers/complex_fluids/upload/Workshop-Booklet-final.pdf.